JAMES | Journal of Advances in Modeling Earth Systems

RESEARCH ARTICLE
10.1029/2020MS002453

Two-Moment Bulk Cloud Microphysics With Prognostic Precipitation in GFDL's Atmosphere Model AM4.0: Configuration and Performance

Huan Guo[1], Yi Ming[1], Songmiao Fan[1], Linjiong Zhou[1,2], Lucas Harris[1], and Ming Zhao[1]

[1]NOAA/Geophysical Fluid Dynamics Laboratory, Princeton, NJ, USA, [2]Cooperative Institute for Modeling the Earth System, Program in Oceanic and Atmospheric Sciences, Princeton University, Princeton, NJ, USA

Key Points:

- Two-moment microphysics with prognostic precipitation and ice nucleation schemes have been implemented in Atmosphere Model version 4.0 (AM4.0), referred to as AM4-MG2
- The overall skill scores of AM4-MG2 are close to AM4.0
- Improvements include better coastal stratocumulus, more realistic liquid and ice partitioning, dominant accretion over autoconversion

Correspondence to:
H. Guo,
huan.guo@noaa.gov

Citation:
Guo, H., Ming, Y., Fan, S., Zhou, L., Harris, L., & Zhao, M. (2021). Two-moment bulk cloud microphysics with prognostic precipitation in GFDL's Atmosphere Model AM4.0: Configuration and performance. *Journal of Advances in Modeling Earth Systems*, *13*, e2020MS002453. https://doi.org/10.1029/2020MS002453

Received 23 DEC 2020
Accepted 17 MAY 2021

Abstract A two-moment Morrison-Gettelman bulk cloud microphysics with prognostic precipitation (MG2), together with a mineral dust and temperature-dependent ice nucleation scheme, have been implemented into the Geophysical Fluid Dynamics Laboratory's Atmosphere Model version 4.0 (AM4.0). We refer to this configuration as AM4-MG2. This paper describes the configuration of AM4-MG2, evaluates its performance, and compares it with AM4.0. It is shown that the global simulations with AM4-MG2 compare favorably with observations and reanalyses. The model skill scores are close to AM4.0. Compared to AM4.0, improvements in AM4-MG2 include (a) better coastal marine stratocumulus and seasonal cycles, (b) more realistic ice fraction, and (c) dominant accretion over autoconversion. Sensitivity tests indicate that nucleation and sedimentation schemes have significant impacts on cloud liquid and ice water fields, but higher horizontal resolution (about 50 km instead of 100 km) does not.

Plain Language Summary We have implemented a sophisticated cloud microphysical scheme in the Geophysical Fluid Dynamics Laboratory's Atmosphere Model AM4.0. This microphysical scheme predicts both mass and number concentrations of cloud droplets, ice crystals, rain, and snow. Additionally, the nucleation of mineral dust aerosols to ice crystals has been considered as part of an effort to represent aerosol-cloud-ice interactions more realistically. We conducted multi-year global simulations. Simulation results turn out to be in good agreement with observations, and show improvements in coastal stratocumulus, cloud liquid and ice phase partitioning, and the ratio of accretion (collection of cloud drops by raindrops) over autoconversion (collision and coalesce between droplets to form raindrops).

1. Introduction

Clouds play critical roles in global energy budget and hydrology cycles, but their representation in general circulation models (GCMs) remains a major source of uncertainties (IPCC and Stocker, 2013). One large uncertainty resides in the impacts of aerosols on clouds (also known as aerosol indirect effects). Aerosols can affect cloud drop and ice crystal number concentrations via the activation process (Twomey, 1974). Furthermore, they can influence precipitation formation, and cloud lifetime or liquid water path via collision, coalescence, and collection processes (Albrecht, 1989). These processes involve cloud drops and ice crystals ranging from less than a micrometer to a few millimeters. Given the large grid spacings (on the order of 100 km), the microphysical processes have to be parameterized in GCMs.

The cloud microphysics parameterizations have evolved quickly in recent decades. More sophisticated cloud microphysical schemes (for example, two-moment, prognostic precipitation) are available and have been implemented in global models (e.g., Gettelman & Morrison, 2015; Gettelman et al., 2015; Ghan et al., 1997; Lohmann et al., 1999; Morrison & Gettelman, 2008; Salzmann et al., 2010; Walters et al., 2014). Two-moment bulk cloud microphysics schemes predict both mass mixing ratio and number concentration in most cases. They allow the number concentration (or particle size) to evolve consistently with the mass mixing ratio, and represent the aerosol-cloud interactions more realistically than one-moment (mass only) schemes that prescribe the number concentration or particle size.

A recent model development study indicated that Morrison and Gettelman (2008) two-moment bulk cloud microphysics scheme (MG1 hereafter) improved coastal stratocumulus simulations in the Geophysical

Fluid Dynamics Laboratory (GFDL)'s Atmosphere Model version 3 (AM3) (Guo et al., 2014). The lack of coastal stratocumulus is a persistent bias in the GFDL global models (Donner et al., 2011; GFDL Global Atmosphere Model Development Team, 2004; Horowitz et al., 2020; Zhao et al., 2018a), as well as a number of other state-of-the-art GCMs (Golaz et al., 2019; Kelley et al., 2020; Voldoire et al., 2019). The insufficient stratocumulus clouds allow too much shortwave absorption by the underlying ocean, and develop positive sea surface temperature (SST) biases and impact seasonal SST cycles (Gordon et al., 2000). Large and Danabasoglu (2006) pointed out that the SST biases were related to excess precipitation in the Southern Hemisphere tropics, that is, "double" intertropical convergence zone (ITCZ). Therefore, the improved coastal stratocumulus could have significant implications for fully coupled simulations. As stressed by Donner et al. (2011), it is a high priority to improve the representations of the coastal marine stratocumulus for future model development.

The prognostic treatment of precipitation promotes accretion but reduces autoconversion (Gettelman & Morrison, 2015; Posselt & Lohmann, 2008, 2009; Walters et al., 2014). Autoconversion is often parameterized as a function of drop number concentration. The overestimate of autoconversion is possibly one reason why the aerosol indirect effects are amplified in many GCMs (Quaas et al., 2009; Wang et al., 2012). Prognostic precipitation is expected to enhance the ratio of accretion over autoconversion, and alleviate the over-prediction of the aerosol indirect effects. Gettelman et al. (2015) reported that the aerosol indirect effects could be weakened by 30%, after the prognostic precipitation treatment described in Gettelman and Morrison (2015) (MG2 hereafter) was introduced in the Community Atmosphere Model, version 5 (CAM5).

Aerosol activation is a key bridge between aerosols and clouds. Compared to the parameterizations of drop activation that are more physically based (Ghan et al., 2011; Ming et al., 2006), the parameterizations of ice nucleation are less constrained. The nucleated ice crystal concentrations could differ by an order of magnitude or more, leading to a wide spread in cloud water phase (liquid and ice partitioning) simulations among GCMs (Komurcu et al., 2014). The wide spread could introduce a large uncertainty in quantifying cloud feedback, because the partitioning between cloud liquid and ice would affect both precipitation efficiency and radiative properties of mixed phase clouds (McCoy et al., 2016; Zhao, 2014). As an effort to advance the cloud phase simulations and aerosol-cloud-ice representations, Fan et al. (2019) developed a mineral dust and temperature-dependent nucleation scheme, and showed that it could potentially ameliorate the over-estimation of ice fraction in the GFDL Atmosphere Model version 4.0 (AM4.0).

In order to narrow down the uncertainty of the aerosol indirect effects, and to improve the coastal stratocumulus and cloud water phase simulations, we implemented MG2, along with a dust and temperature-dependent ice nucleation scheme, in AM4.0 (hereafter AM4-MG2). This paper documents the implementation and performance of AM4-MG2. We provide brief descriptions of AM4.0 and AM4-MG2 in Section 2. Section 3 evaluates the AM4-MG2 global simulation results (including model mean climate, and cloud microphysical, and macrophysical properties) against observations and reanalyses, and compares them with AM4.0 results. Section 4 estimates aerosol radiative flux perturbation (RFP) and examines primary rain formation processes: autoconversion and accretion. Section 5 investigates the model sensitivity to sedimentation scheme, ice nucleation scheme, and refined horizontal resolution. Finally, we summarize our findings in Section 6.

2. Model Description and Configuration

2.1. Brief Description of AM4.0

AM4.0 (Zhao et al., 2018a, 2018b) was based upon AM3 (Donner et al., 2011) and the High Resolution Atmospheric Model (HiRAM) (Zhao et al., 2009), but with new features in dynamic core and especially in physics packages. The dynamic core adopts the hydrostatic version of the GFDL Finite-Volume Cubed-Sphere Dynamical Code (FV3) (Harris, Zhou, Chen et al., 2020; Lin, 2004; Putman & Lin, 2007). A new "double-plume" convective closure parameterizes both shallow and deep convection (Zhao et al., 2016, 2018b). An updated topographic gravity drag scheme is built on an analytical expression for arbitrary topography and then expanded to include nonlinear effects (Garner, 2005, 2018). A "light" chemistry disables photochemistry and stratospheric chemistry to speed up simulations, but it is capable of simulating aerosols from emissions using prescribed oxidants (Held et al., 2019; Zhao et al., 2018a). Note that the prescribed oxidant

Table 1
Comparison of Cloud Microphysical and Aerosol Activation Schemes in AM4-MG2 and AM4.0

	AM4-MG2	AM4.0
microphysics	two-moment Morrison-Gettelman with prognostic precipitation (MG2) (Gettelman & Morrison, 2015)	[a] one-moment+ Rotstayn-Klein with diagnostic precipitation (RK) (Rotstayn, 1997; Jakob & Klein, 2000)
[b]drop activation	mechanistic (Ming et al., 2006, 2007)	mechanistic (Ming et al., 2006, 2007)
ice nucleation	dust and temperature-dependent for prognostic ice number concentration (Fan et al., 2019)	only temperature-dependent, only for Wegener–Bergeron–Findeisen process (Meyers et al., 1992)

[a]RK cloud microphysical scheme predicts both mass mixing ratio and number concentration of cloud liquid drops, but only mass mixing ratio of cloud ice. In other words, it is a one-moment scheme with the exception of two-moment in cloud liquid. [b]The minimum standard deviation of sub-grid vertical velocity probability density function (PDF) for cloud drop activation is reduced to 0.3 m s^{-1} in AM4-MG2 from 0.7 m s^{-1} in AM4.0.

concentrations are based on full chemistry simulations. The model is topped at 1 hPa, which is referred to as "low top". There are fewer vertical levels (i.e., coarse vertical resolution) in the stratosphere in AM4.0 than AM3. Thus, the representation of the stratosphere is limited. The radiative transfer codes have substantial modifications, for example, adding 10 μm CO_2 band and re-fitting to line-by-line benchmark simulations (Pincus et al., 2020).

The representations of planetary boundary layer (PBL), cloud macrophysics, and cloud microphysics in AM4.0 remain almost unchanged from AM3. The PBL scheme considers down-gradient eddy diffusion with diffusivities following Lock et al. (2000). The cloud macrophysics with prognostic cloud fraction is parameterized according to Tiedtke (1993). In our implementation, super-saturation over ice is allowed (Salzmann et al., 2010). The cloud microphysical scheme was originally a one-moment bulk scheme. It only prognosed the mass mixing ratios of cloud water and ice, while rain and snow were diagnosed, following Rotstayn (1997) with modifications in mixed-phase clouds (Rotstayn et al., 2000) and in the overlap between clouds and precipitation (GFDL Global Atmosphere Model Development Team, 2004; Jakob & Klein, 2000). Later the microphysical scheme has been updated to predict cloud droplet number concentration since AM3 (Donner et al., 2011), with drop activation dependent on updrafts and aerosol chemical and size properties in order to facilitate the study of aerosol-cloud interactions (Golaz et al., 2011; Ming et al., 2006, 2007). We refer to this as Rotstayn-Klein (RK) cloud microphysical scheme hereafter (See Table 1). A detailed description of AM4.0 is documented in Zhao et al. (2018a, 2018b).

2.2. Brief Description and Configuration of AM4-MG2

AM4-MG2 is based on AM4.0, but replaces the RK microphysics with the MG2 microphysics. MG2 assumes that cloud particles follow gamma distributions, and predicts the mass mixing ratios and number concentrations (i.e., two moments) of cloud water and ice (Morrison & Gettelman, 2008; Gettelman et al., 2008). Moreover, the prognostic equations are extended to include the two moments of precipitation: rain and snow (Gettelman & Morrison, 2015; Gettelman et al., 2015). Because of the fast fall velocity of precipitation species, there often exist numerical stability problems when applying prognostic precipitation in GCMs. Many state-of-the-art GCMs have vertical spacing of ~100 m in the planetary boundary layer (Danabasoglu et al., 2020; Gettelman et al., 2015; Golaz et al., 2019; Zhao et al., 2018a). For example, stratiform rain could fall down at 2–4 m s^{-1} (Niu et al., 2010). This requires a time step of 25–50 s to satisfy the Courant-Friedrichs-Lewy (CFL) stability criterion if we employ an explicit sedimentation scheme. Unfortunately, such a short time step is not ideal for GCMs given the current computational power. One solution is to substep the sedimentation time step as implemented in CAM5 (Gettelman et al., 2015). Another approach is to employ an implicit sedimentation scheme. In this study, we apply a time-implicit scheme to the sedimentation of both number and mass of all hydrometeors. The implicit scheme is vastly simpler and more stable. It

does not require substepping, and is more efficient computationally (Harris, Zhou, Lin, et al., 2020; Zhou et al., 2019).

2.2.1. Radiative Properties of Rain and Snow

The radiative effects of both rain and snow are taken into account in AM4-MG2. The shortwave optical properties of rain were derived from Mie theory assuming that raindrops followed a lognormal distribution. The extinction coefficient depends on rain water content and effective radius. The single scattering albedo and asymmetry factor are parameterized for four spectral bins as a function of rain effective radius (Savijärvi, 1997). The shortwave properties of snow are parameterized for six spectral bins as a function of snow water content only (Fu et al., 1995). The longwave properties of rain and snow were derived assuming that rain and snow were spherical particles. The radiative properties at 12 infrared bands only depend on their mass mixing ratios, not their particle sizes (Fu et al., 1995). We did sensitivity tests with and without the radiative effects of rain and snow, and found that they had little impact on the results of this study. Therefore, we will not discuss them further.

2.2.2. Ice Nucleation

AM4-MG2 predicts both droplet and ice number concentrations. Since ice nucleation is a dominant source for ice crystals, its parameterization is critical for simulating mixed-phase and cirrus clouds. Ice crystals can form through either homogeneous nucleation or heterogeneous nucleation. In this study, the homogeneous nucleation is parameterized based on Koop et al. (2000). The heterogeneous nucleation at $T < 233$ K is parameterized based on Ullrich et al. (2017, 2019) for mineral dust and soot particles, but is neglected for sea-salt and organic/sulphate particles. For the heterogeneous nucleation at $T > 233$ K, we adopt a mineral dust and temperature-dependent scheme developed by Fan et al. (2019). This scheme is based on parcel model simulations, and is well-constrained by laboratory experiments and in situ aircraft measurements (Fan et al., 2017).

The nucleated ice crystal number concentration, N_i^* (in units of cm^{-3}), is obtained via a least squares fitting to the parcel model results

$$N_i^* = A_{fit}[dust]e^{0.412(273.15-T)}\frac{p}{95000}10^{-6} \quad (1)$$

where A_{fit} is a proportionality coefficient, $[dust]$ mineral dust mass concentration ($\mu g\ m^{-3}$), T air temperature (K), p pressure (Pa). A_{fit} is set to 5.48 in AM4-MG2, doubled from 2.74 in Fan et al. (2019), to account for a similar increase of ice nucleation active sites from the empirical parameterization of Niemand et al. (2012) to Ullrich et al. (2017) based on the experiments with desert dust particles.

To be consistent with ice mass mixing ratio, the ice number concentration is also subject to large-scale transport, turbulence mixing, and convective detrainment. In this study, the ice number detrainment is parameterized as a function of detrained ice mass mixing ratio and temperature (Kristjansson et al., 2000; Salzmann et al., 2010).

Unlike in AM4-MG2, the ice number concentration is used in AM4 only for the representation of Wegener–Bergeron–Findeisen (WBF) process that is essential for mixed-phase clouds. The ice number concentration is approximated by N_i^*, and N_i^* is parameterized following Meyers et al. (1992) (see Table 1),

$$N_i^* = 0.001e^{[12.96(273.15-T)/80-0.639]} \quad (2)$$

Note that the Meyers et al. (1992) scheme is used in AM4.0 only for the WBF parameterization, but it is not used in AM4-MG2 (Table 1).

3. Global Simulation Results and Evaluations

The global results in this section are from AMIP (Atmospheric Model Intercomparison Project) mode simulations with AM4-MG2 and AM4.0, where sea surface temperature (SST) and sea ice are prescribed (Gates, 1992; Gates et al., 1999). The horizontal grids have cubed-sphere topology with six faces and 96×96

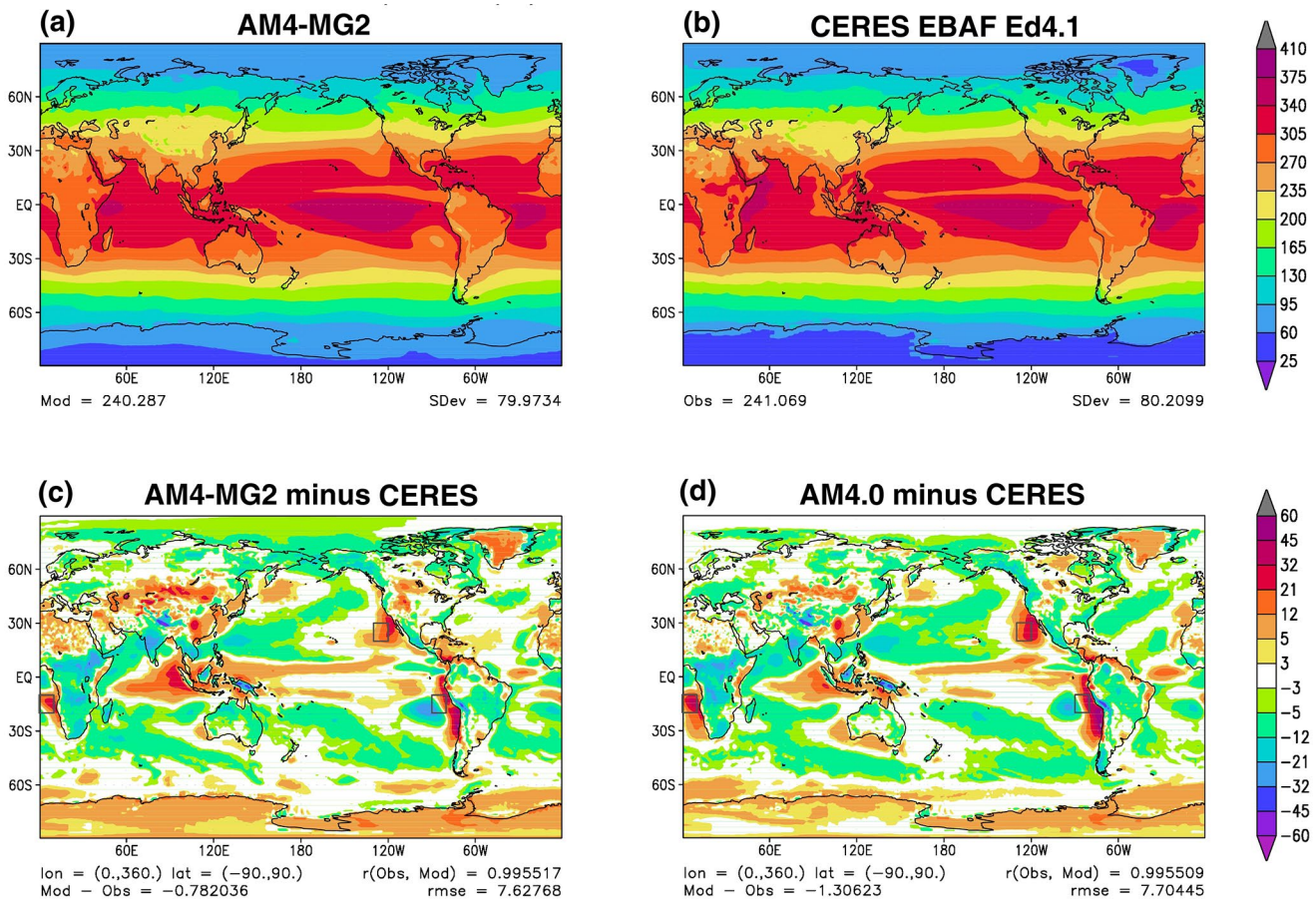

Figure 1. Annual-mean net downward shortwave flux or shortwave absorption (SWABS, W m^{-2}) at the top-of-atmosphere (TOA) from (a) AM4–MG2 averaged over 1980–2014, (b) CERES–EBAF Ed4.1 averaged over 2000–2015, (c) AM4–MG2 model error (AM4-MG2 minus CERES), and (d) AM4.0 (averaged over 1980–2014) model error. The boxes indicate subtropical stratocumulus regions: Peruvian [80°W–90°W, 10°S–20°S], Namibian [0°E–10°E, 10°S–20°S], and Californian [120°W–130°W, 20°N–30°N] regions as defined in Klein and Hartmann [1993].

points on each face, corresponding to a nominal horizontal resolution of about 1° or 100 km. There are 33 vertical levels with a sponge layer extending from model top (at 1 hPa) to 8 hPa. The physical time step is 30 min with two substeps for the microphysical processes. The simulation period is from January 1, 1979 to December 31, 2014. The first year is considered as a spin-up, and the climatology for the period 1980–2014 is analyzed here. Additional sensitivity tests are discussed in Section 5.

3.1. Mean Model Climate

3.1.1. Shortwave Absorption and Marine Stratocumulus

Our evaluations of AM4-MG2 performance start with radiative fluxes at the top-of-atmosphere (TOA) because the observational estimates are well constrained and the radiative balance is of significance for atmosphere-ocean fully coupled simulations (Zhao et al., 2018a). Figure 1a shows the annual mean net downward shortwave flux or shortwave absorption (SWABS) global map at TOA from AM4-MG2. The satellite observations are based on the Clouds and the Earth's Radiant Energy System-Energy Balanced and Filled climatology Edition 4.1 (CERES-EBAF-Ed4.1) (Figure 1b) (Loeb et al., 2009, 2018). It is clear that the SWABS spatial pattern from AM4-MG2 compares well with CERES-EBAF-Ed4.1. AM4-MG2 shows better agreement with the observations over the mid-latitude oceans (the North Pacific, North Atlantic, Southern Ocean) than AM4.0. But it exhibits larger biases over the tropical Indian Ocean and the tropical western Pacific.

Table 2
Summary of Annual Mean Bias and Root Mean Square Error (RMSE, in Parenthesis) of Shortwave Absorption (SWABS) at the Top-of-Atmosphere (TOA) From AM4.0 and AM4-MG2 Relative to CERES-EBAF-Ed4.1 Over Three Representative Stratocumulus Regions and Three Extended Stratocumulus Regions

	AM4.0	AM4-MG2
	($W\ m^{-2}$)	($W\ m^{-2}$)
Peruvian [80–90°W, 10–20°S]	10.8 (21.0)	−0.1 (16.3)
Namibian [0–10°E, 10–20°S]	23.8 (25.5)	14.7 (17.8)
Californian [120–130°W, 20–30°N]	19.2 (20.1)	12.3 (13.2)
extended Peruvian [70–90°W, 10–30°S]	16.6 (28.1)	6.8 (21.6)
extended Namibian [0–10°E, 10–30°S]	16.9 (19.9)	6.5 (13.2)
extended Californian [110–130°W, 10–30°N]	11.1 (14.4)	8.6 (11.0)

AM4-MG2 and AM4.0 share negative biases over sub-Saharan Africa and western Pacific storm track regions, suggesting excessive cloudiness. Positive biases occur along the west coasts of South America, Africa, and North America, indicating insufficient coastal marine stratocumulus there. But AM4-MG2 ameliorates the positive biases. As shown in three representative stratocumulus regions near Peru [80°W–90°W, 10°S–20°S], Namibia [0°E–10°E, 10°S–20°S], and California [120°W–130°W, 20°N–30°N] (i.e., boxed regions in Figures 1c and 1d), the positive biases are less pronounced ("reddish") in AM4-MG2 than AM4.0. The annual mean biases over three stratocumulus regions are −0.1, 14.7, and 12.3 W m^{-2} in AM4-MG2, which are about 10 W m^{-2} in magnitude smaller than those in AM4.0 (Table 2). The corresponding root mean square errors (RMSEs) are 16.3, 17.8, and 13.2 W m^{-2} in AM4-MG2, also smaller than those in AM4.0 by 5–8 W m^{-2}. However, it might be argued that the smaller bias (−0.1 W m^{-2}) over the Peruvian region is largely caused by the cancellation between positive and negative bias (Figure 1). In order to reduce the cancellation error, we re-calculate the mean biases and RMSEs over three extended stratocumulus regions with latitude/longitude bounds at [70°W–90°W, 10°S–30°S] [0°E–10°E, 10°S–30°S], and [110°W–130°W, 10°N–30°N]. It turns out that the mean biases and RMSEs are reduced by 3–10 W m^{-2} in AM4-MG2, compared to those in AM4.0 (Table 2). The reduced model errors over the stratocumulus regions are encouraging, especially because the insufficient coastal stratocumulus clouds are a long-standing problem in GFDL global models including AM2, AM3, and AM4.0, and because the insufficiency could negatively impact the ITCZ and El Niño-Southern Oscillation (ENSO) simulations in the coupled mode (Gordon et al., 2000; Large & Danabasoglu, 2006).

Figure 2 shows the spatiotemporally averaged vertical profiles of cloud fraction, liquid water content, and longwave radiative cooling from AM4-MG2 and AM4.0 near Peru, Namibia, and California. The observational estimates of cloud fraction and liquid water content are provided by a merged product of CALIPSO (Cloud-Aerosol Lidar and Infrared Pathfinder Satellite Observations), CloudSat, CERES, MODIS (Moderate Resolution Imaging Spectroradiometer) retrievals (C3M) (Kato et al., 2010). AM4-MG2 and AM4.0 generate too little cloud fraction and too thin a cloud layer. Their peak cloud fractions are only about half of the C3M observations (Figures 2a, 2d and 2g). Nevertheless, the simulated clouds appear to have maximum

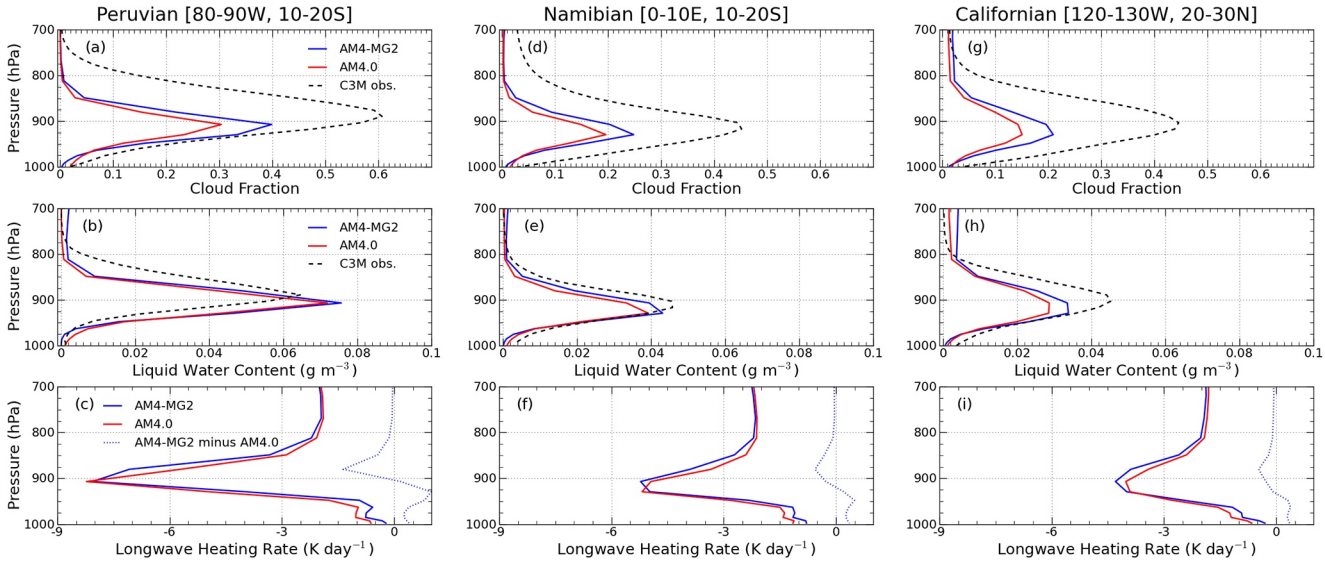

Figure 2. Vertical profiles of annual mean cloud fraction (%), liquid water content (g m^{-3}), and longwave radiative heating rate (K day^{-1}) over the Peruvian, Namibian, and Californian regions from AM4-MG2 and AM4.0 averaged from 1980 to 2014; and cloud fraction and liquid water content from CALIPSO, CloudSat, CERES, MODIS (C3M) observations averaged from 2006 to 2011 (Kato et al., 2010). The heating rate difference between AM4-MG2 and AM4.0 is shown in (c) (f) (i).

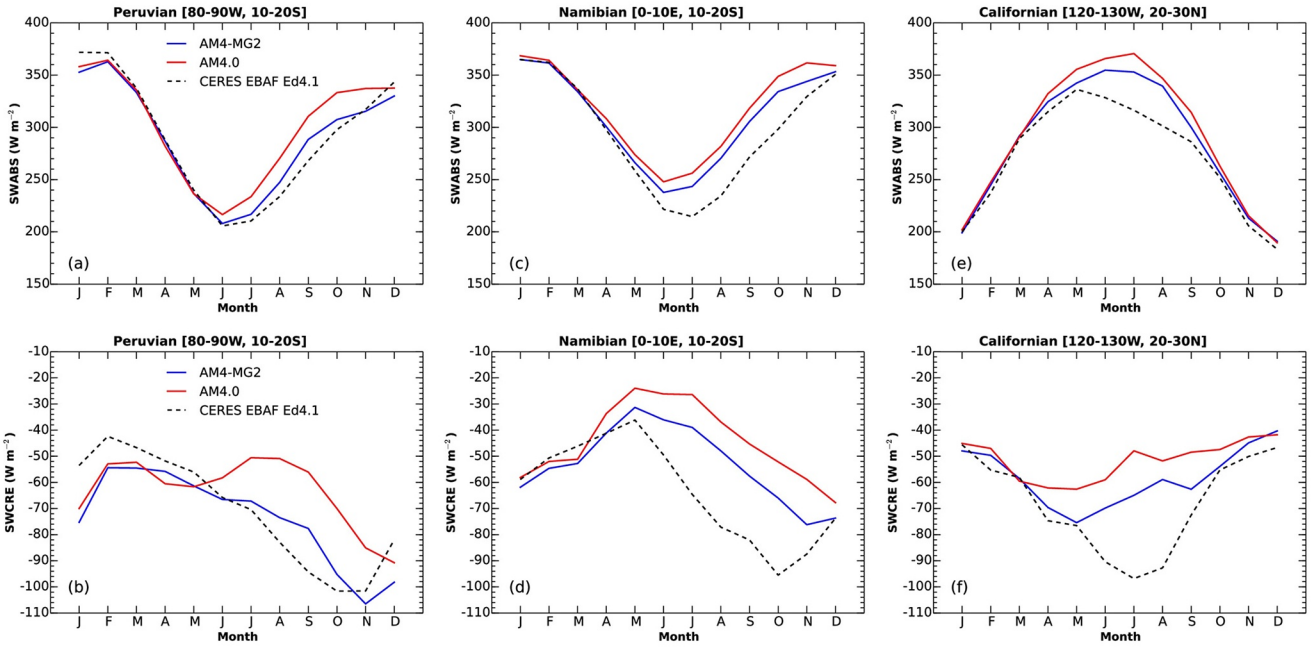

Figure 3. Seasonal shortwave absorption (SWABS, W m^{-2}), and cloud radiative effect (SWCRE, W m^{-2}) for AM4-MG2 (blue), AM4.0 (red), and CERES-EBAF Ed4.1 (black) over the Peruvian region in (a) and (b), the Namibian region in (c) and (d), and the Californian region in (e) and (f).

cloud water content comparable to observations (Figures 2b, 2e and 2h). This indicates that the positive biases in SWABS (Figures 1c and 1d) are largely due to the modeled stratocumulus clouds that are too low in coverage and are too shallow in depth. Clearly AM4-MG2 produces higher cloud fraction and liquid water content than AM4.0 in the three regions (Figure 2), resulting in smaller (positive) biases in SWABS (Figures 1c and 1d).

For the cloud fraction in these stratocumulus regions where large-scale subsidence is prevalent, cloud top radiative cooling is an important source (Tiedtke, 1993). The cooling at the top sustains a turbulence-driven and well-mixed stratocumulus boundary layer, and the sustained stratocumulus clouds in turn strengthen the longwave radiative cooling. It is a positive feedback. Therefore, thicker stratocumulus clouds are often associated with stronger cooling, and vice versa. Consistent with higher cloud fraction and cloud water content, the cloud top radiative cooling is also stronger in AM4-MG2. It is stronger by up to 1.36 K day^{-1} (or 24%), 0.56 K day^{-1} (or 17%), and 0.47 K day^{-1} (or 14%) in Peruvian, Namibian, and Californian regions, respectively (Figures 2c, 2f and 2i).

The SWABS and shortwave radiative effect (SWCRE) of the subtropical stratocumulus clouds undergo significant seasonal cycles. The highest SWABS and the strongest (the most negative) SWCRE tend to occur in local summer or autumn, and the lowest SWABS and the weakest SWCRE happen during local winter or spring (Figure 3). In the Peruvian region, AM4-MG2 behaves similarly to CERES-EBAF-Ed4.1. The SWABS reaches its maximum (360 W m^{-2}) and minimum (210 W m^{-2}) in austral summer and winter, respectively. The SWCRE peaks and bottoms at about −55 W m^{-2} and −105 W m^{-2} in austral fall and spring, respectively. Although the SWABS from AM4.0 is in fair agreement with CERES-EBAF-Ed4.1, the SWCRE is not. It exhibits double peaks in March and August, which is unexpected. Moreover, its magnitude tends to be smaller than AM4-MG2 and CERES-EBAF-Ed4.1, especially in austral winter and spring (Figures 3a and 3b). The stratocumulus clouds in the Namibian region demonstrate similar seasonal cycles to those in the Peruvian region (Figures 3c and 3d). Both AM4-MG2 and AM4.0 are able to capture the overall trends of seasonal variations in SWABS and SWCRE, but the magnitudes in AM4-MG2 are closer to CERES-EBAF-Ed4.1, especially during austral winter and spring.

The seasonal cycles in the Californian region are opposite to those in the Peruvian and Namibian regions. The highest SWABS and the most negative SWCRE occur in boreal summer, and the lowest SWABS and the

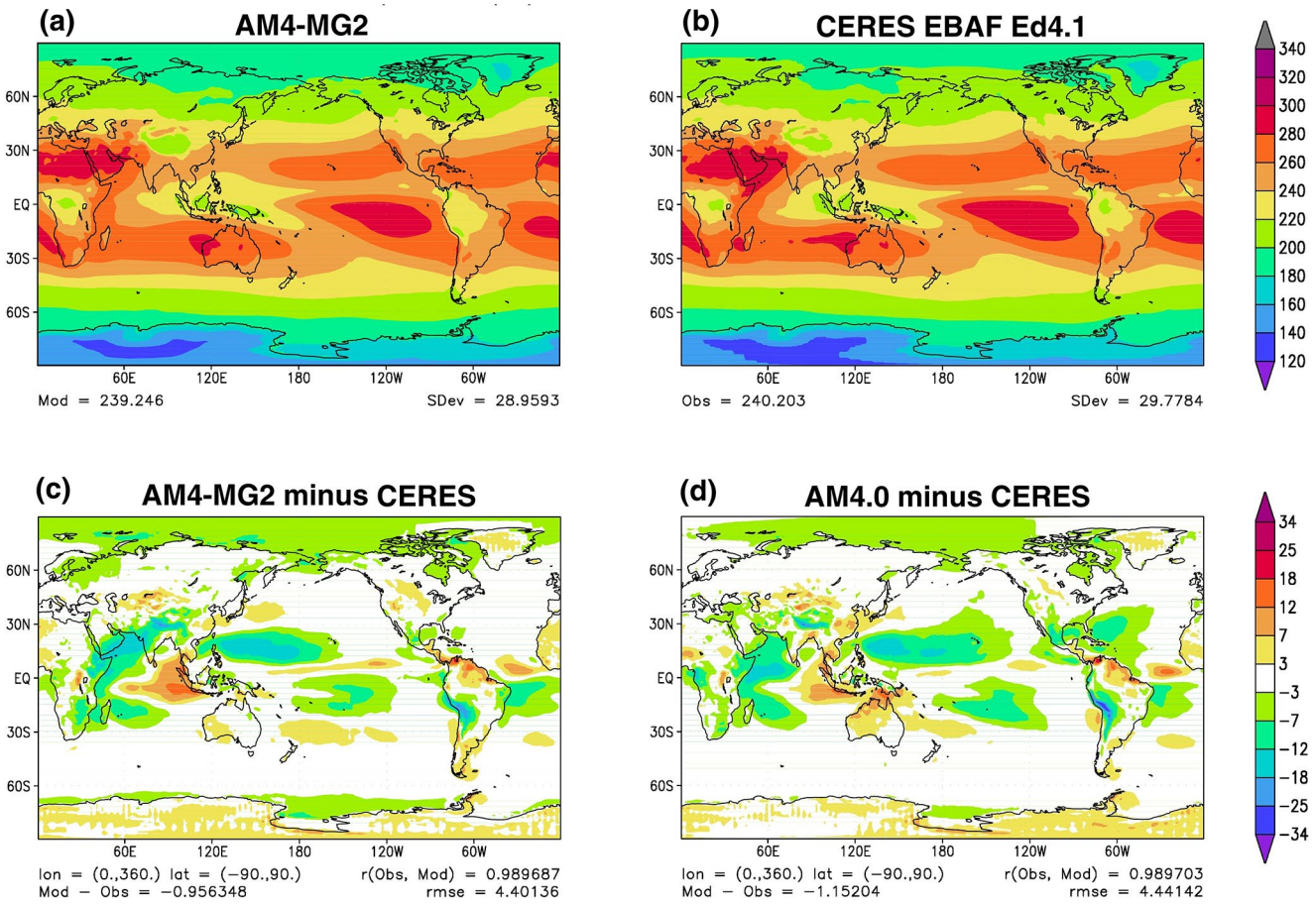

Figure 4. As in Figure 1 but for the top-of-atmosphere (TOA) outgoing longwave radiation (OLR, W m^{-2}).

least negative SWCRE take place in boreal winter (Figures 3e and 3f). Both AM4-MG2 and AM4 tend to underestimate the magnitude of SWCRE. But AM4-MG2 shows stronger (more negative) SWCRE, consistent with higher cloud amount and water content (Figures 2g and 2h). Overall, AM4-MG2 performs better than AM4.0 in simulating the phase and amplitudes of the seasonal cycles of the radiative properties of coastal stratocumulus clouds.

3.1.2. Outgoing Longwave Radiation

Figure 4 displays the global maps of annual-mean outgoing longwave radiation (OLR). The OLR spatial pattern from AM4-MG2 agrees well with the observational reference (CERES-EBAF-Ed4.1). At first glance, the bias pattern from AM4-MG2 is close to that from AM4.0 with comparable global RMSE (4.40 vs. 4.44 W m^{-2}). Both models show negative biases over the West Indian Ocean, the tropical Pacific, the tropical Northwest Atlantic, and the Arctic; and positive biases over East Indian Ocean. A closer look reveals that over these tropical ocean regions, the negative biases are weaker (less "bluish") and the positive biases are stronger (more "reddish") in AM4-MG2 (Figures 4c and 4d). This implies that AM4-MG2 likely has less high level clouds there. One reason is due to stronger convection (or more convective precipitation). The ratio of convective precipitation over total precipitation in AM4-MG2 is 0.46, but it is lower (0.40) in AM4.0. A comprehensive investigation of convection under the AM4-MG2 framework is beyond the scope of this study. The interactions between convection and large-scale stratiform clouds warrant future research.

3.1.3. Precipitation

The climatology of total surface precipitation rates from AM4-MG2 and observations can be found in Figures 5a and 5b. The Global Precipitation Climatology Project Version 2.3 (GPCP V2.3) data set serves as the observational guidance in this paper (Adler et al., 2003, 2016). Compared to the GPCP V2.3, both AM4-MG2

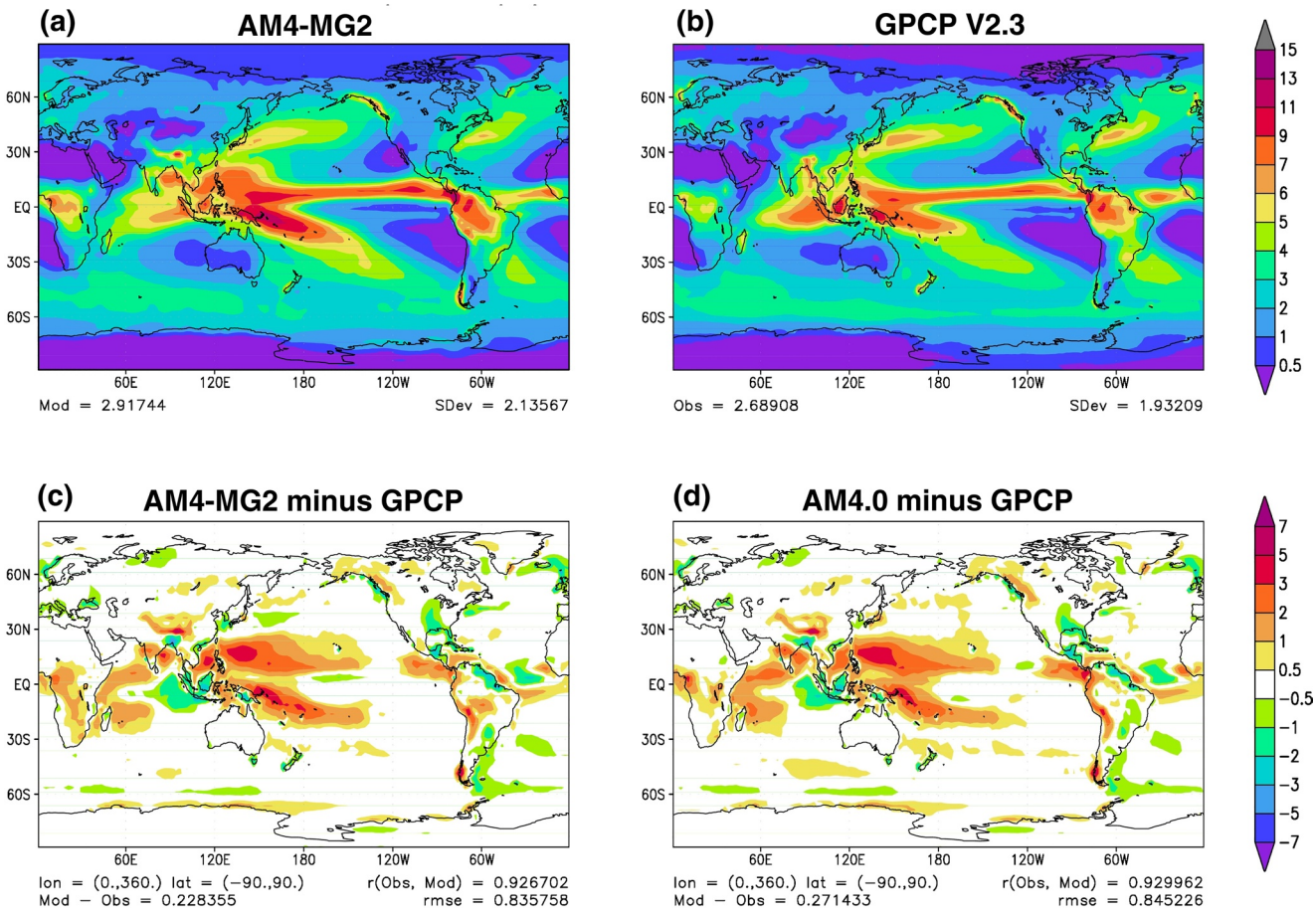

Figure 5. Annual-mean surface precipitation rate (mm day^{-1}) for (a) AM4–MG2 averaged for the 1980–2014 period, (b) GPCP v2.3 averaged for the 1980–2015 period, (c) AM4–MG2 model error (AM4-MG2 minus GPCP), and (d) AM4.0 (averaged for the 1980–2014 period) model error.

and AM4.0 overestimate the surface precipitation (by about 10%), as illustrated by the prevailing positive (wet) biases in Figures 5c and 5d. The global means from AM4-MG2 and AM4.0 are 2.92 mm day^{-1} and 2.96 mm day^{-1}, respectively, but it is only 2.69 mm day^{-1} from the GPCP V2.3. Nevertheless, the observational estimates are subject to large uncertainties (Gehne et al., 2016; Sun et al., 2018). The precipitation is likely underestimated by ~10% over tropical oceans, and by a higher percentage over mid-latitude oceans (Stephens et al., 2012). The global mean precipitation rate from the ERA-Interim reanalysis is about 2.92 mm day^{-1} (Dee et al., 2011), the same as the AM4-MG2 value.

The global RMSEs are comparable (0.84 mm day^{-1} in AM4-MG2 versus 0.85 mm day^{-1} in AM4.0) (see Figures 5c and 5d). Removing the global mean bias, the standard deviations become 0.81 mm day^{-1} for AM4-MG2 and 0.80 mm day^{-1} for AM4.0. The model biases mainly show up in the tropics. There are wet biases in the tropical Pacific and West Indian Ocean and dry biases in the East Indian Ocean, which are consistent with the OLR bias patterns in Figure 4. AM4-MG2 has wetter Southern Africa and drier East Indian Ocean than AM4.0. These tropical biases are expected to be closely related to the convection parameterization, and the interactions between convection and large-scale stratiform clouds (Zhao et al., 2018a, 2018b).

A more detailed examination is conducted by analyzing the precipitation partitioning. As shown in Figure 6, the tropical precipitation is dominated by convective precipitation, while the precipitation in the mid-latitudes mainly comes from large-scale stratiform precipitation. AM4-MG2 produces more convective precipitation, albeit less large-scale precipitation. During the development of AM4-MG2, we increased the lateral mixing for the deep plume to 1.1 from 0.9 (as used in AM4.0), with the purpose to weaken the convection. But it turns out that the convection is still stronger than that in AM4.0. We noticed that the large-scale precipitation was also reduced after the MG1 microphysics was implemented in AM3 (See stratiform

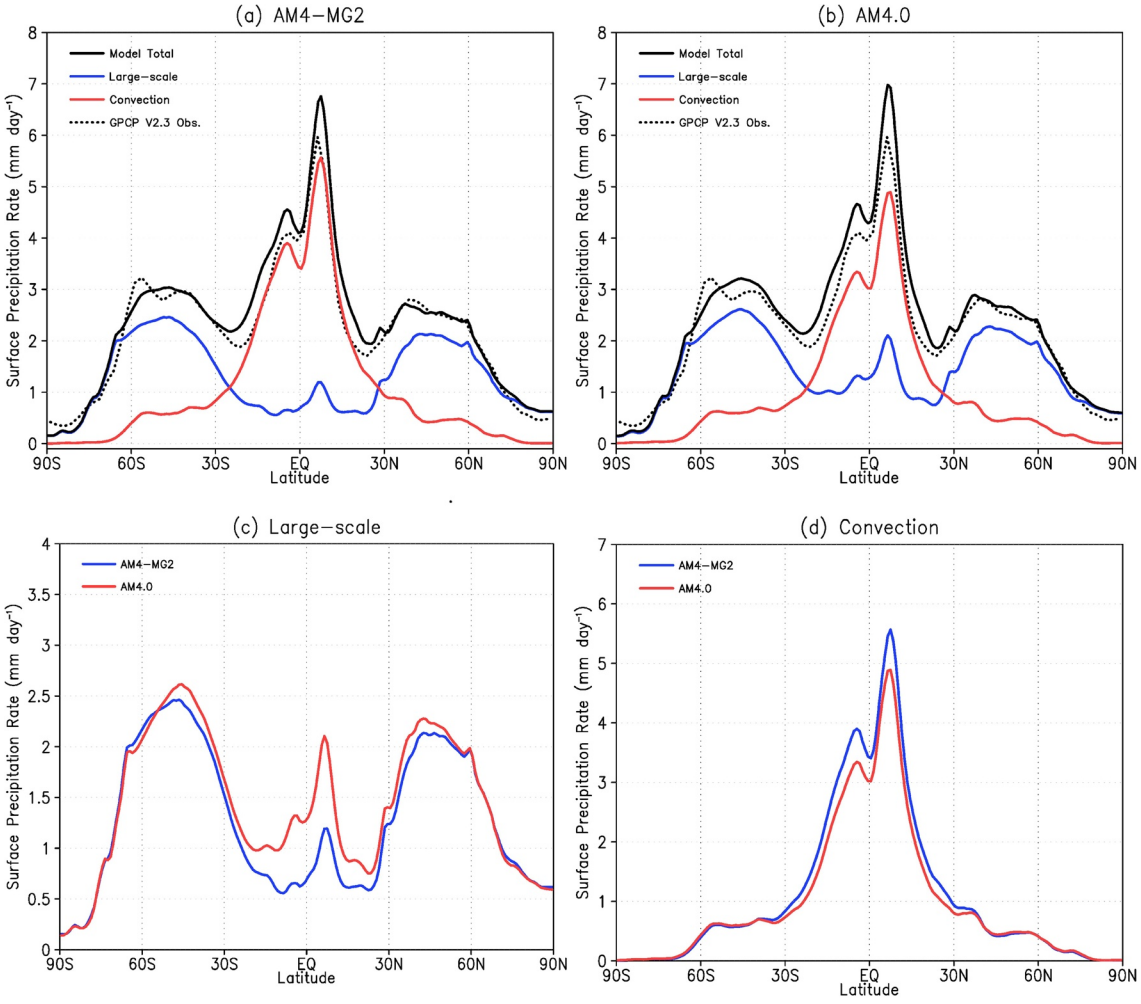

Figure 6. Zonal-mean precipitation partitioning (mm day^{-1}) for (a) AM4-MG2 and (b) AM4.0, large-scale stratiform and convective precipitation in (c) and (d).

precipitation P_{strat} in Table 2 in [Salzmann et al., 2010]). The convective precipitation and large-scale precipitation have changed after the RK microphysics is replaced by the MG1 or MG2 microphysics.

The MG2 microphysics precipitates less readily than the RK microphysics. The cloud microphysics precipitation efficiency, which is defined as the ratio of surface precipitation rate to the sum of column-integrated vapor condensation and deposition rates (Sui et al., 2005, 2007), is lower (0.56 in AM4-MG2 versus 0.66 in AM4.0). AM4-MG2 thus has a lower large-scale stratiform precipitation rate (Figure 6c and Table 3). Because the large-scale stratiform precipitation is less efficient in removing water vapor, the environmental relative humidity becomes higher. A higher relative humidity may favor the development of convective precipitation (Figure 6d), and more active convection.

Figure 7a demonstrates the precipitation intensity distributions from AM4-MG2, AM4.0, and the Tropical Rainfall Measuring Mission (TRMM) 3B42(V7) observation (Huffman et al., 2007). The distributions were sampled over 3-hourly surface precipitation rate for the latitude band from 50°S to 50°N, which the TRMM data set covers. The distribution is for the period of 1998–2001 from TRMM, and for the period of 1980–2014 from AM4-MG2 and AM4.0, respectively. The modeled distributions overall compare well with the TRMM distribution. Both AM4-MG2 and AM4.0 are able to capture the major feature of the distribution: the stronger the precipitation, the less frequently it occurs. Both models overestimate the occurrence of precipitation rate <30 mm day^{-1}, and underestimate the occurrence of precipitation >30 mm day^{-1}. The AM4-MG2 distribution almost overlaps with the AM4.0 one, except for slightly lower occurrence of

Table 3
Global-Annual Mean AM4-MG2 and AM4.0 Results for 1980–2014, and Observations: Aerosol Optical Depth (AOD) Estimate is Based on the Multi-Angle Imaging SpectroRadiometer (MISR) Data (Diner et al., 1998; Kahn et al., 2005, 2009); Low, Medium, High, and Total Cloud Amount (LCA, MCA, HCA, TCA) Based on CloudSat-CALIPSO; Shortwave Cloud Radiative Effect (SWCRE), Longwave Cloud Radiative Effect (LWCRE), Based on CERES-EBAF Ed4.1 (Loeb et al., 2018); Water Vapor Path (WVP) Based on the NASA Water Vapor Project (NVAP) Total Column Water Vapor Data Sets; Convective and Stratiform Liquid Water Path (LWP_{cw}) Over Ocean Based on the Multi-Sensor Advanced Climatology of Liquid Water Path (MAC-LWP) (Elsaesser et al., 2017); Total Ice Water Path (IWP_{tot}) Based on the CloudSat (Jiang et al., 2012); Sea Level Pressure (SLP) at Arctic, Northern Hemisphere (NH), Southern Hemisphere (SH), 250 hPa, 850 hPa Temperature and U-Wind (T200, T850, U200, U850) Based on ERA-Interim (Dee et al., 2011); 2-m Air Temperature (T_{ref}) Over Land Based on Climate Research Unit (CRU) (Brohan et al., 2006)

Variable	Observations	AM4-MG2	AM4.0
AOD	0.17	0.15	0.15
AOD ocean	0.16	0.13	0.14
LCA (%)	43.0	36.0	32.2
MCA (%)	32.2	17.3	15.5
HCA (%)	40.3	45.1	37.8
TCA (%)	66.8	67.2	61.0
SWCRE (W m^{-2})	−45.4	−48.2	−48.6
LWCRE (W m^{-2})	25.9	22.7	23.7
WVP (g m^{-2})	24.7	24.5	23.6
[a]LWP_{cw} ocean (g m^{-2})	81.1	74.5	60.7
[b]LWP_{tot} (g m^{-2})		98.8	59.8
stratiform cloud water		61.7	49.4
stratiform rain		25.4	-
convective cloud water		11.7	10.4
[c]IWP_{tot} (g m^{-2})	70.1	53.8	53.5
stratiform cloud ice		27.8	[d]52.7
stratiform snow		25.4	-
convective cloud ice		0.6	0.8
[e]P_{strat} (mm day^{-1})		1.32	1.55
SLP Arctic (hPa)	1,013	1,013	1,012
SLP NH (hPa)	1,014	1,013	1,013
SLP SH (hPa)	1,009	1,008	1,008
T250 (K)	225.8	225.3	224.8
T850 (K)	281.6	281.3	281.5
U250 (m s^{-1})	14.5	14.5	14.7
U850 (m s^{-1})	1.15	1.05	1.03
T_{ref} land	13.5	13.1	12.9

[a]LWPcw includes both stratiform and convective cloud water, but not rain. [b]LWPtot includes stratiform and convective cloud water, and rain. [c]IWPtot includes stratiform and convective cloud ice, and snow. [d]stratiform cloud ice in AM4.0 includes both stratiform cloud ice and snow. [e]Pstrat is large-scale stratiform precipitation rate at surface.

precipitation rate higher than 100 mm day^{-1}, consistent with lower mean surface precipitation rate (Figures 6a and 6b).

Figure 7b compares the distributions of large-scale and convective precipitation intensity from AM4-MG2 and AM4.0. In AM4-MG2, large-scale precipitation occurs less frequently, and convective precipitation occurs more frequently. This is in line with the weaker large-scale precipitation but stronger convective precipitation after the MG2 microphysics is introduced (Figures 6c and 6d), confirming that the MG2 scheme is less likely to generate precipitation than the RK scheme.

3.1.4. Global Mean Climatological Skill

An overview of global annual means of variables from AM4-MG2 and AM4.0 is provided in Table 3. The global mean aerosol optical depths (AODs) from models agree well with the Multi-angle Imaging SpectroRadiometer (MISR) estimates (Diner et al., 1998; Kahn et al., 2005, 2009). AM4-MG2 has more high-level cloud amount than AM4.0 globally, but its longwave radiative effect (LWCRE) is lower by 1 W m^{-2} . One reason is the higher water vapor content. The water vapor path (WVP) is 24.5 g m^{-2} and 23.6 g m^{-2} for AM4-MG2 and AM4, respectively (Table 3). Given more vapor, the clear-sky OLR (OLR_clr) at TOA is effectively coming from higher altitude and colder temperature, and thus lower. As a result, the LWCRE (LWCRE = OLR_clr - OLR) is lower, too.

The liquid water path due to stratiform and convective clouds (LWP_{cw}) over the ocean is underestimated. The underestimation of LWP is a common problem shared by a number of state-of-the-art GCMs including high resolution models (Jing et al., 2017). Compared to AM4.0, AM4-MG2 alleviates such bias. The LWP in AM4-MG2 is higher by more than 20%, and closer to the observational reference provided by the Multi-Sensor Advanced Climatology of Liquid Water Path (MAC-LWP) (Elsaesser et al., 2017). The total LWP (LWP_{tot}) from AM4-MG2 is not comparable to that from AM4.0, because the former includes rain while the latter does not. Consistent with LWP_{cw}, the global mean stratiform and convective LWP are higher in AM4-MG2, due to higher stratiform LWP.

The total ice water path (IWP_{tot}) and the convective IWP from AM4-MG2 and AM4.0 have similar magnitudes. Unlike AM4.0, which merges ice and snow into one prognostic variable, AM4-MG2 predicts ice and snow separately. As a result, the stratiform IWP from AM4-MG2 is not comparable to that from AM4.0. The modeled thermodynamic and momentum fields: sea level pressure, temperature, and U-wind at different pressure levels are close to the ERA-Interim reanalyses (Dee et al., 2011).

A summary of the global climatology performance is given by target diagrams in Figure 8 (Jolliff et al., 2009). Target diagrams manifests the differences between models and observations/reanalyses in a compact but clear fashion. The *y*-axis and *x*-axis represent the normalized model bias and unbiased root-mean-square difference (RMSD), respectively. The closer to the origin, the better the agreement between models and observations/reanalyses. For these 12 climatically important fields, AM4-MG2 and AM4.0 tend to be clustered together. The overall model skill scores of two models are similar, although the LWCRE looks slightly different due to the reason discussed earlier.

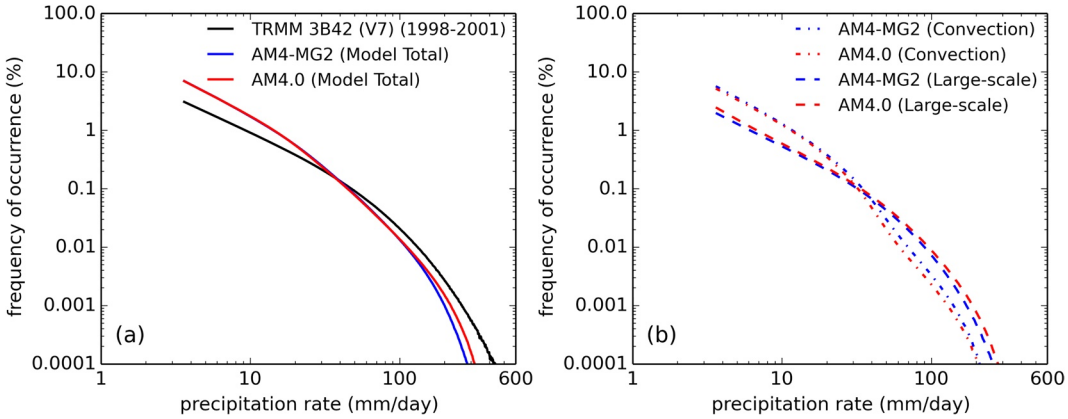

Figure 7. Precipitation intensity distributions between [50°S, 50°N] from TRMM, AM4-MG2, and AM4.0 in (a), and large-scale and convective precipitation intensity distributions from AM4-MG2, and AM4.0 in (b). Note that the distributions from AM4-MG2, and AM4.0 are for the period of 1980–2014.

3.2. Cloud Microphysical Properties

3.2.1. In-Cloud Drop and Ice Size and Number Concentration Probabilities

Figure 9 displays the relative frequencies of occurrence of drop effective radius and in-cloud drop number concentration over the ocean and land, sampled over the instantaneous cloud fields with liquid water content above 10^{-6} kg m^{-3}. The modeled drop size tends to be smaller over land than over the ocean,

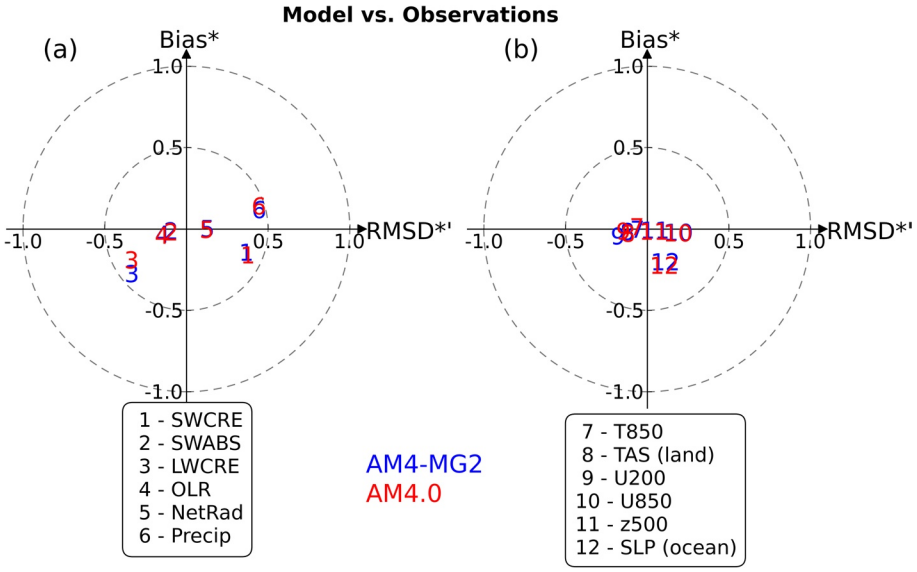

Figure 8. Target diagrams showing AM4-MG2 (blue) and AM4.0 (red) model performance. Model results are annual-means for the 1980–2014 period. Vertical axis (Bias*-axis) and horizontal axis (RMSD$^{*'}$-axis) are model bias and unbiased root-mean-square difference (RMSD), respectively. Note that both model bias and RMSD are normalized by the spatial standard deviations of references (i.e., observations and/or reanalyses). If the spatial standard deviation of model variables is greater than that of references, RMSD$^{*'}$ is positive, otherwise, RMSD$^{*'}$ is negative. Fields shown are shortwave cloud radiative effect (SWCRE), shortwave absorbed radiation (SWABS), longwave cloud radiative effect (LWCRE), outgoing longwave radiation (OLR), net radiation (NetRad), precipitation (Precip), geopotential height at 500 hPa (z500), temperature at 850 hPa (T850), surface air temperature over land (TAS (land)), zonal-wind at 200 hPa and 850 hPa (U200 and U850), and sea level pressure (SLP), Observations of SWCRE, SWABS, LWCRE, and OLR are from CERES-EBAF Ed4.1 (Loeb et al., 2018), precipitation from GPCP V2.3 (Adler et al., 2003, 2016), surface temperature from Climate Research Unit (CRU) (Brohan et al., 2006), and sea level pressure, geopotential height, wind, temperature from 40-year European Center for Medium-Range Weather Forecasts (ECMWF) Re-Analysis (ERA-40) (Uppala et al., 2005).

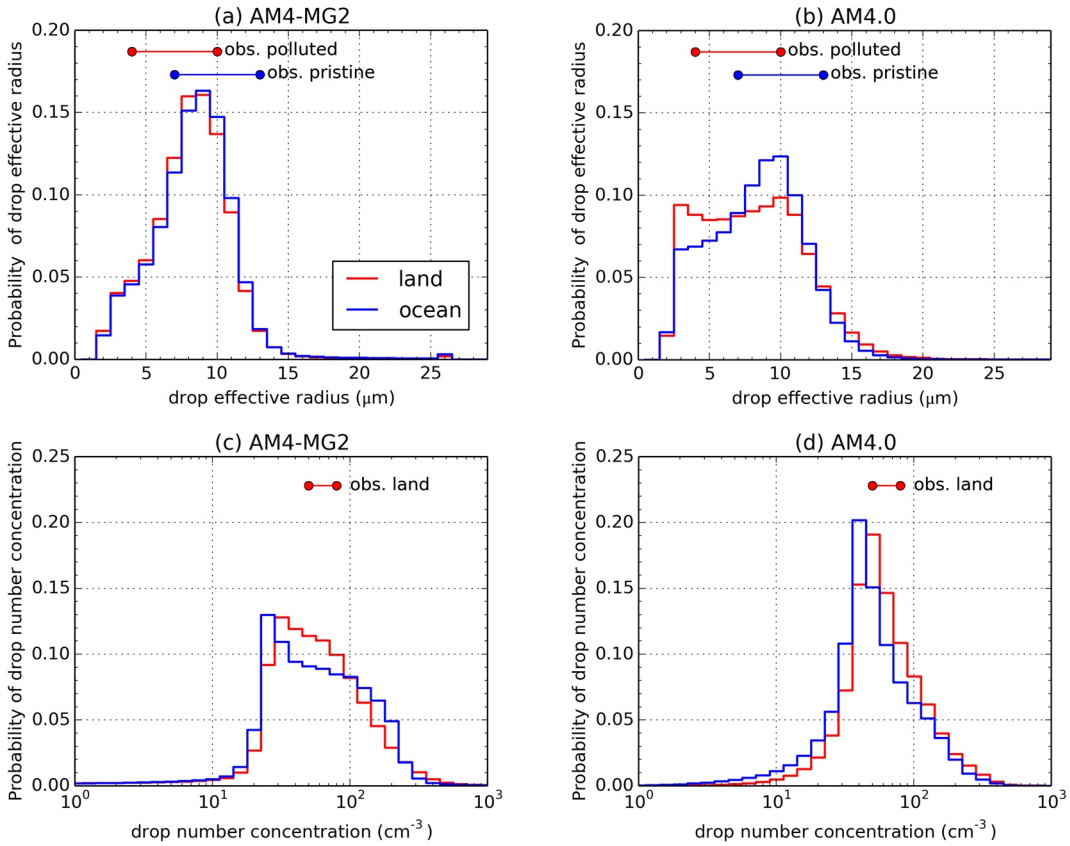

Figure 9. Global probability of cloud droplet effective radius and in-cloud drop number concentration over land and over ocean for clouds with liquid water content higher than 10^{-6} kg m^{-3}. The observed effective radius in pristine and polluted conditions ranges from 7 to 13 μm, and from 4 to 10 μm, respectively. The observed drop number concentration over land varies from 50 to 80 cm^{-3}.

while the drop number concentration is higher over land than over the ocean. The modeled effective radius mostly falls in the range of 2–15 μ m. These values compare well with the in-situ measurements: from about 7 to 13 μ m for clean clouds, and from about 4 to 10 μ m for polluted clouds, respectively (Bower & Choularton, 1992; Brenguier & Schüller, 2003; Gettelman et al., 2008; Martin et al., 1994; Pawlowska and Brenguier, 2006; Salzmann et al., 2010). The simulated drop number concentration is likely between 10 and 300 cm^{-3} with peaks around 30–100 cm^{-3}, which agrees with the continental cloud observations of 50–80 cm^{-3} (Gettelman et al., 2008; Gultepe & Isaac, 2004).

The relative frequencies of occurrence of drop effective radius and number concentration from AM4-MG2 and AM4.0 are different. There are more small drops with radius between 2 and 5 μ in AM4.0 (Figure 9b). One reason is the inclusion of super-cooled liquid drops (Salzmann et al., 2010). The super-cooled clouds are often associated with lower liquid water content and thus smaller drops. The other reason is probably the autoconversion parameterization. In AM4.0, the autoconversion representation follows Manton and Cotton (1977), which requires the drop size to reach a threshold (8.5 μm) to trigger precipitation. Otherwise, the conversion of cloud water to rain water is inactive. Consequently, the smaller drops are more likely to survive. The threshold-based scheme, however, is not realistic. Given the disperse drop distribution, the collision and coalescence process always occurs. AM4-MG2 employs the Seifert and Beheng [2001] autoconversion scheme that was derived from stochastic collection equations. It considers the continuous collision and coalescence allowing cloud drops to grow and form rain. The clouds dominated by small drops (e.g., below 5 μm) are less common in AM4-MG2.

We notice a kink around 25 μm in AM4-MG2 (Figure 9a). The reason is because the drop radius is limited between 1 and 25 μm (Morrison & Gettelman, 2008). In case that the drop radius is beyond the specified

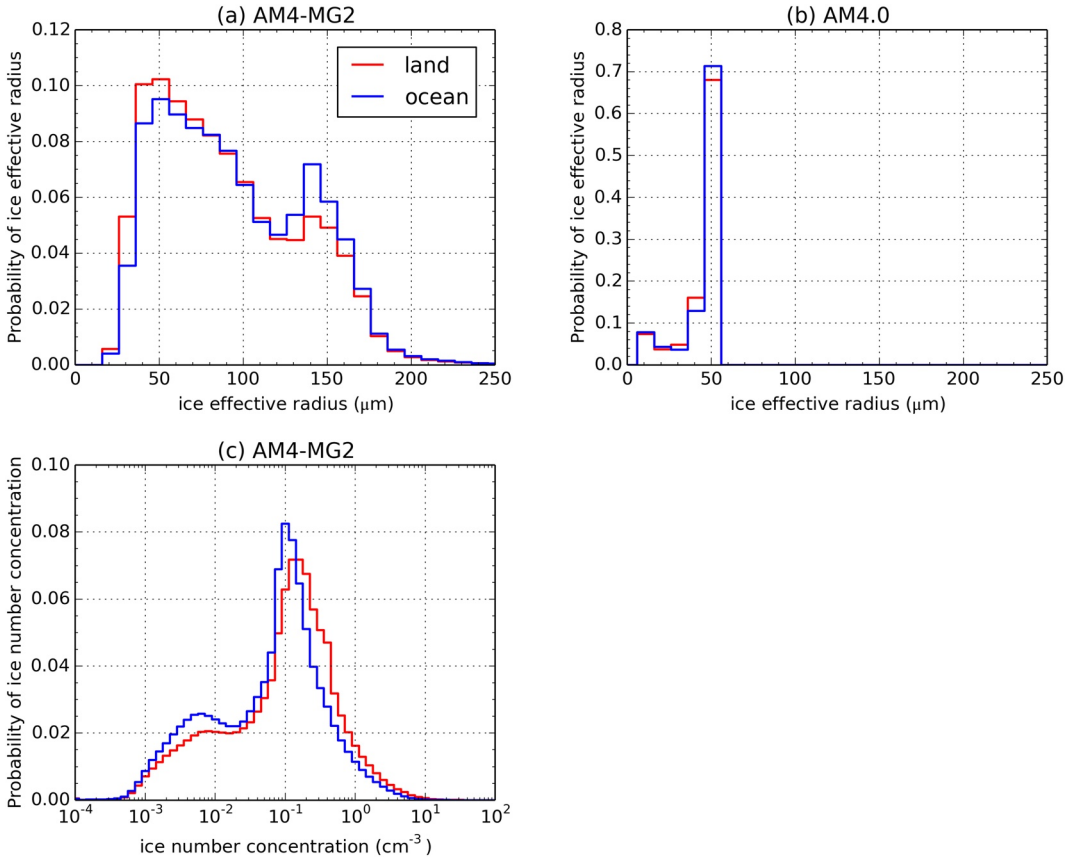

Figure 10. Global probability of cloud ice effective radius and in-cloud ice number concentration over land and over ocean for clouds with ice water content higher than 10^{-6}kgm^{-3}. Note that ice number concentration is not considered and thus the probability of ice number concentration is unavailable in AM4.0.

limits, we adjust the drop number concentration without modifying the cloud water content. This drop number adjustment also partly explains why there is a lower possibility of drop number concentration below 20 cm^{-3} in AM4-MG2 (Figure 9c).

The relative frequencies of occurrence of ice effective radius and in-cloud ice particle number concentration can be found in Figure 10. Similar to Figure 9, Figure 10 also applies the threshold of 10^{-6} kg m^{-3} for ice water content when sampling. In AM4.0, the ice crystal effective radius is diagnosed as a step function of temperature (Donner et al., 1997), based on observations by Heymsfield and Platt (1984). The diagnosed effective radius varies between 10 and 50 μm and peaks around 50 μm (Figure 10b). The ice number is not considered explicitly in AM4.0, so its frequency is unavailable.

As expected, AM4-MG2 shows a clear land-sea contrast. The ice particle number concentration peaks near 0.15 cm^{-3} over the land and 0.1 cm^{-3} over the ocean (Figure 10c). This indicates the sensitivity of ice clouds to aerosol loading. The ice particle size seems to have two modes. One is around 50 μm, and the other is around 150 μm. The maximum ice particle size is limited by the conversion threshold of ice to snow (Morrison & Gettelman, 2008; Gettelman et al., 2008).

3.3. Cloud Macrophysical Properties

This section mainly examines cloud water phase (i.e., liquid-ice partitioning). We use ice cloud "occurrence frequency" phase ratios (FPR) data retrieved from the Global Climate Model-Oriented CALIPSO Cloud Product (GOCCP) as observational guidance (Chepfer et al., 2010). The satellite data are based on lidar backscattering measurements. The lidar signal is sensitive to ice but does not penetrate optically thick clouds. A lidar simulator is ideal to assist the classification of simulated clouds (Cesana et al., 2015). But we

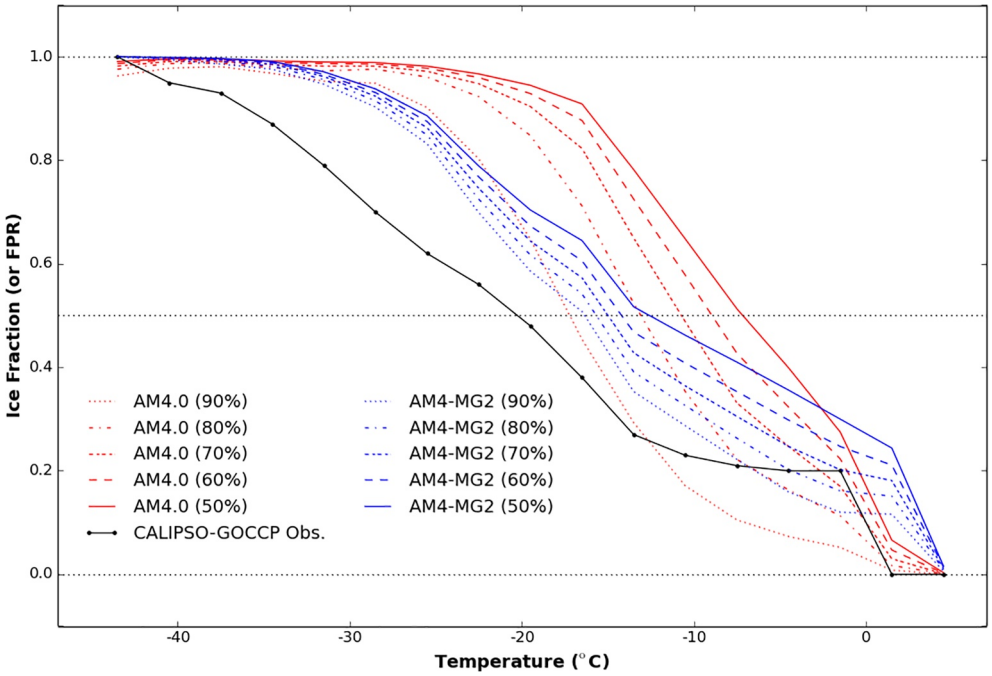

Figure 11. Ice fraction (or occurrence frequency phrase ratio, FPR) versus temperature from CALIPSO-GOCCP observations (black), and from AM4-MG2 (blue) and AM4.0 (red) at five different thresholds for identifying ice clouds. If ice (including snow if available) mass fraction is higher than a threshold (e.g., 50%), it is tagged as an ice cloud; otherwise, it is a liquid cloud. The CALIPSO-GOCCP FPR data are averaged over different temperature bins from 2007 to 2011. The ice fractions from AM4-MG2 and AM4.0 are estimated by sampling over daily instantaneous three-dimensional cloud liquid, ice, and snow (if available) fields for 2008. Note that sampling different years yield almost the same estimates of ice fraction.

choose to use mass fraction to quantify the cloud phase partitioning, following Komurcu et al. (2014). An ice mass fraction threshold is applied to determine ice clouds (Fan et al., 2019). If the ice (including snow if available) mass fraction ($\frac{\text{ice mass}}{\text{ice mass + liquid mass}}$) exceeds the specified threshold, then the clouds are tagged as ice clouds. Otherwise, they are liquid clouds. Following Fan et al. (2019), we estimate the ice fractions in AM4-MG2 and AM4.0 at five different thresholds (50%, 60%, 70%, 80%, and 90%). Obviously, the higher the threshold, the lower the ice fraction.

Figure 11 compares the ice fractions from AM4-MG2 and AM4.0 to CALIPSO-GOCCP FPR. The ice fractions are averages over different temperature bins by sampling over daily instantaneous cloud water, ice, and snow (if available) fields for 2008. CALIPSO-GOCCP FPR comes from global grid-mean observations and then similarly averaged over temperature bins from 2007 to 2011. Although the sampling periods between models and observations are different, this difference has little impact on the estimates of the ice fraction. Overall AM4-MG2 agrees better with the CALIPSO-GOCCP observations, especially for temperature between −30°C and −10°C. It shows a more gradual transition from liquid cloud to ice cloud across the temperature range, and tends to have lower ice fractions than AM4.0 except for the threshold of 90%. The lower ice fraction is consistent with the higher LWP in AM4-MG2 (Table 3), and echoes the similar ice fraction changes reported by Fan et al. (2019) after they replaced Equation 2 with Equation 1 in the WBF parameterization in AM4.0. This comparison implies that ice nucleation (or ice nucleating particles) could impose remarkable impact on the liquid-ice partitioning.

A further analysis is performed by comparing the ice fractions over the Northern and Southern Hemispheres (Figure 12). The Northern Hemisphere has more land mass, therefore, more dust emissions from deserts and/or semiarid regions. Mineral dusts could be one of the most efficient ice nuclei after they are transported and suspended in the atmosphere (Hoose et al., 2008; Hoose & Möhler, 2012). The Southern Hemisphere, however, contains fewer ice nucleating particles. So we expect a higher ice fraction (or lower

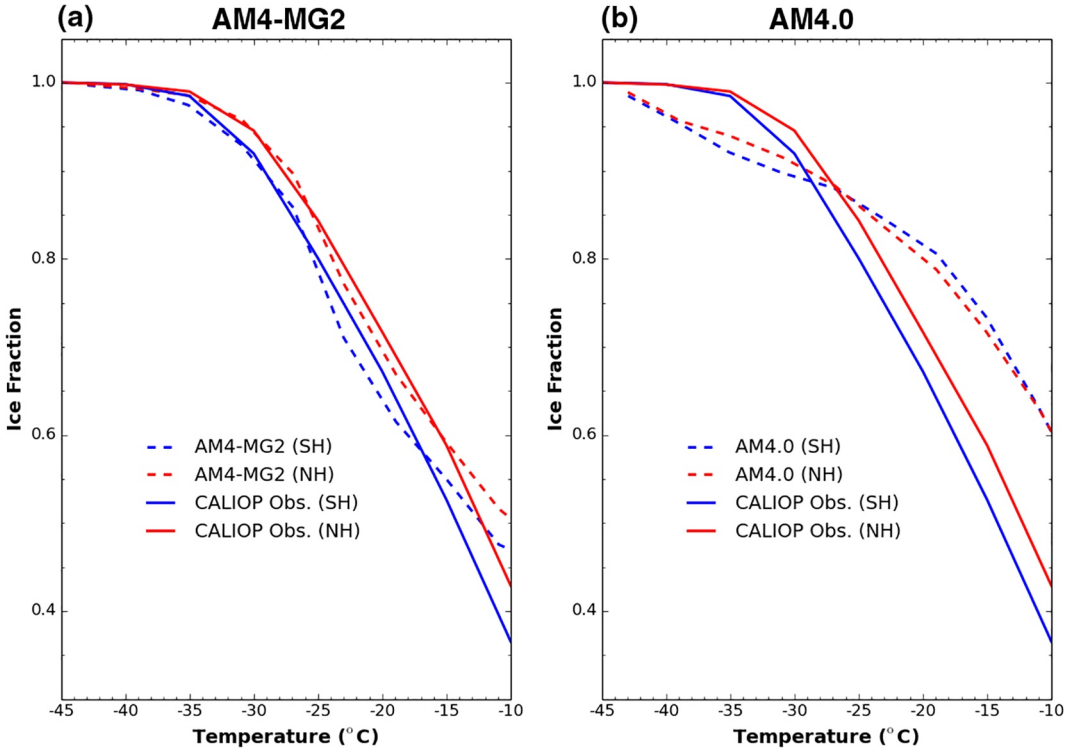

Figure 12. Ice fraction versus temperature over the Northern (0°, 82°N) and Southern (82°S, 0°) Hemispheres. The CALIOP observations are averaged from December 2007 to December 2012 (Tan et al., 2014), and model results from AM4-MG2 and AM4.0 are averaged from January 2008 to December 2012.

supercooled fraction) over the Northern Hemispheres, which is confirmed by the observations based on NASA's Cloud-Aerosol Lidar with Orthogonal Polarization (CALIOP) (Choi et al., 2010; Hu et al., 2010; Tan et al., 2014). Clearly, AM4-MG2 is able to capture this feature. It agrees well with the CALIOP observations. This represents a clear advance compared to AM4.0 (Figure 12). For temperature between −30°C and −10°C, AM4.0 tends to have lower ice fractions over the Northern Hemispheres than the Southern Hemispheres, opposite to the CALIOP observations (Figure 12b); and shows consistently higher ice fraction than the observations, as displayed in Figure 11.

4. Aerosol Radiative Flux Perturbation (RFP)

As discussed in Section 1, one motivation of introducing prognostic precipitation in GCMs is to improve the cloud sensitivity to aerosols. In order to assess this sensitivity, we conducted a set of two 10-year climatological runs: one with present-day (2010) aerosol emissions, the other with pre-industrial (1850) aerosol emissions, while the greenhouse gases (including ozone), sea surface temperature, and sea ice concentration are fixed. The change in net radiation (ΔNetRad) at TOA is defined as aerosol radiative flux perturbation (RFP) (Golaz et al., 2011; Haywood et al., 2009; Lohmann et al., 2010). An important characteristics of AM4.0 is that it shows weaker (or less negative) aerosol RFP than AM3. The weaker RFP is largely due to: (a) horizontal resolution (1° in AM4.0 vs. 2° in AM3), (b) aerosol wet removal by convection, and (c) aerosol activation parameterization. Each contributes to about 10% reduction in the magnitude of the aerosol RFP. More detailed discussion on the aerosol RFP in AM4.0 is available in Zhao et al. (2018b).

The aerosol RFP (or ΔNetRad) here includes the contributions mainly from sulphate, organic carbon, and soot. The effect of including soot is about 0.34 W m^{-2} in AM4-MG2 and 0.40 W m^{-2} in AM4.0. The aerosol RFP increases to −0.62 W m^{-2} in AM4-MG2 from −0.72 W m^{-2} in AM4.0 (Table 4). The increase is dominated by shortwave contribution, and is partly compensated by longwave contribution. The change in the shortwave absorption (ΔSWABS) becomes less negative (an increase of about 0.35 W m^{-2}). The change in

Table 4
Difference Between Present-Day (2010) and Pre-industrial (1850) Aerosol Emission Climatology Runs; ΔLWP_{tot} and ΔIWP_{tot} are the Percent Changes in Total Liquid Water Path (LWP) and Ice Water Path (IWP), Respectively, $\Delta Precip_{tot}$ is the Change in Total Surface Precipitation, ΔCRE is the Change in Cloud Radiative Effect (CRE=SWCRE + LWCRE), ΔNetRad is the Change in Net Radiation (NetRad = SWABS-OLR), Also Known as, Radiative Flux Perturbation (RFP)

	AM4.0	AM4-MG2	AM4-MG2-ExpSed
ΔAOD	0.04	0.05	0.05
ΔLWP_{tot} (%)	+2.83	+0.89	+1.17
ΔIWP_{tot} (%)	−0.06	−1.11	−1.37
$\Delta Precip_{tot}$ (mm day^{-1})	−0.03	−0.03	−0.03
ΔSWCRE(W m^{-2})	−0.10	0.20	0.16
ΔLWCRE(W m^{-2})	−0.08	−0.33	−0.32
ΔCRE(W m^{-2})	−0.18	−0.13	−0.16
ΔSWABS (W m^{-2})	−0.72	−0.37	−0.50
ΔOLR (W m^{-2})	0.00	0.25	0.30
ΔNetRad (W m^{-2})	−0.72	−0.62	−0.80

the shortwave cloud radiative effect (ΔSWCRE) turns from negative to positive (an increase of 0.30 W m^{-2}), which conforms to a weaker liquid water path increase (0.89% vs. 2.83%) and thus, a smaller increase in cloud reflectivity. Clearly in AM4-MG2, the less negative ΔSWABS largely stems from the more positive ΔSWCRE, that is, the aerosol indirect effects.

The more positive ΔSWCRE in AM4-MG2 could be explained by primary rain formation processes: autoconversion and accretion. When the precipitation treatment is shifted from diagnostic to prognostic, the contribution from accretion to rain formation becomes more important. For example, the ratio of global mean vertically integrated accretion rate to global mean vertically integrated autoconversion rate ($\frac{\text{Accr\_col}}{\text{Auto\_col}}$) is 1.29 for AM4-MG2 and 0.61 for AM4.0. Obviously, accretion dominates autoconversion for the rain production in AM4-MG2. Because the representations of accretion (unlike autoconversion) in GCMs are usually independent on cloud drop number concentration, the cloud sensitivity to the cloud drop number or aerosols is expected to be suppressed (Gettelman et al., 2013, 2015; Posselt & Lohmann, 2008, 2009).

We sampled hourly instantaneous three-dimensional autoconversion and accretion rates for October and November 2008 from AM4-MG2 and AM4.0. Following Gettelman et al. (2015), we averaged the modeled process rates between 60°S–60°N, and evaluated them against the estimates based on the VAMOS Ocean–Cloud–Atmosphere–Land Study (VOCALS) observations in October and November 2008 over the Southeast Pacific (Wood et al., 2011). As expected, the ratio of accretion over autoconversion in AM4-MG2 is higher than that in AM4.0 by a factor of two or more, especially for liquid water path lower than 100 g m^{-2} (Figure 13a), mainly resulting from the lower autoconversion rate (Figure 13b). Compared to the VOCALS observations, AM4.0 (like many GCMs) overestimates autoconversion rate, hence underestimates the accretion-to-autoconversion ratio. Although AM4-MG2 shares similar biases, it alleviates these biases to some extent, and agrees better with the observations. The accretion rates in AM4-MG2 and AM4 have similar magnitudes, and compare reasonably well with the observational estimates (Figure 13c).

5. Sensitivity to Sedimentation, Ice Nucleation, and Horizontal Resolution

In addition to the base simulations discussed in Section 3, we performed three sensitivity tests to explore the impacts of sedimentation scheme, ice nucleation scheme, and horizontal resolution (Table 5). Note that there is only one change in each test while other model set-ups (including tunings) remain the same, so that we can evaluate differences caused by the single change. The sensitivity tests are historical AMIP mode simulations from 1979 to 2014. The zonal means over 1980–2014 are compared in Figure 14.

In the sensitivity test of AM4-MG2-ExpSed, the explicit (substepping) sedimentation scheme is adopted (Gettelman et al., 2015), instead of the time-implicit method. The explicit scheme removes hydrometeor faster. For large hydrometeor species such as ice, rain, and snow, sedimentation is an important or dominant sink. The stronger the sedimentation, the less these species. This explains why the IWP goes down (Figure 14d). On the other hand, less rain and snow lead to less accretion, riming, and WBF depletion of cloud water. The accretion, riming, and Bergeron processes outweigh the sedimentation for depleting cloud water. Consequently, we see substantially higher LWP and stronger (more negative) SWCRE (Figures 14a and 14c).

Given the strong LWP increase in AM4-MG2-ExpSed, we estimate the liquid water removal time scale ($\tau = \frac{\text{LWP}}{\text{precipitation}}$), which could approximate the liquid cloud lifetime to some degree (Ma et al., 2015). τ is about 51.7 min in AM4-MG2-ExpSed and 48.8 min in AM4-MG2. Longer lifetime allows aerosols to

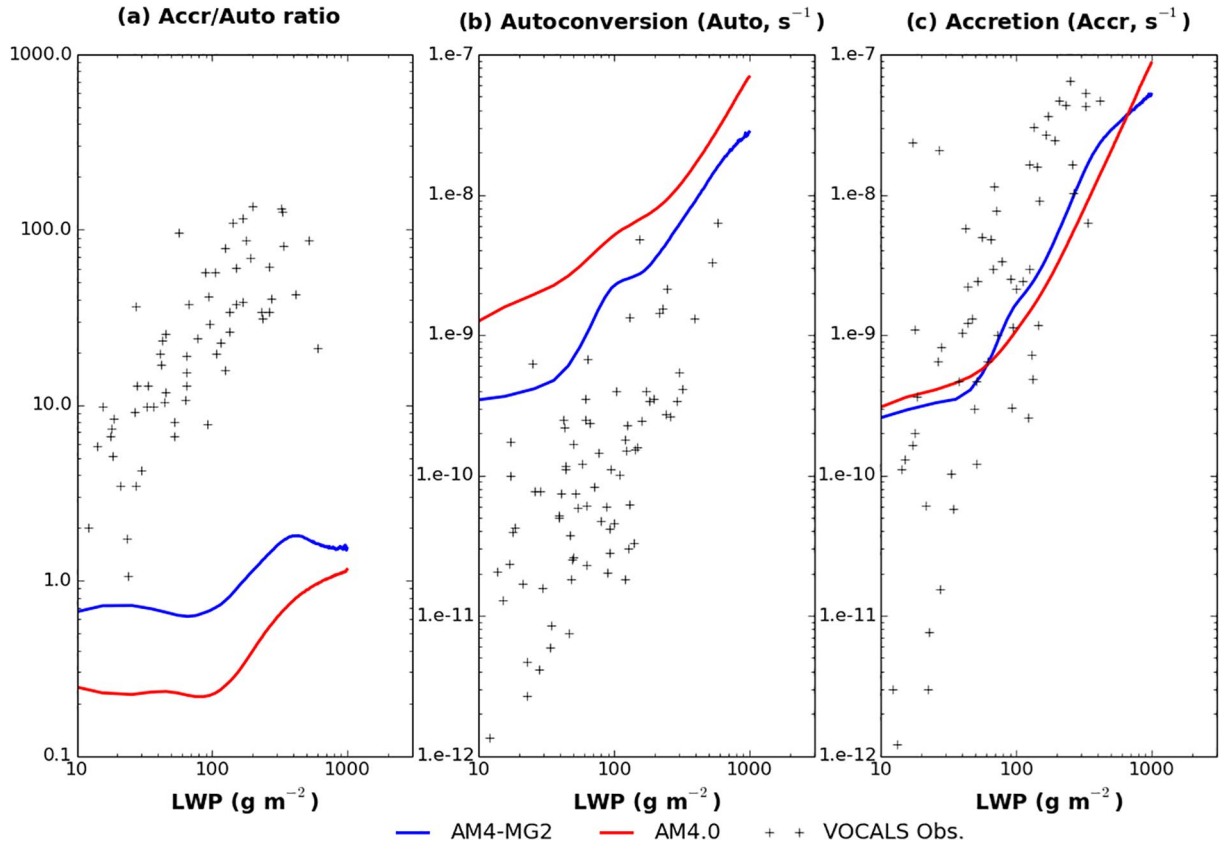

Figure 13. The ratio of accretion to autoconversion in (a), autoconversion rate in (b), and accretion rate in (c) versus stratiform liquid water path (LWP) from AM4-MG2 (blue), AM4.0 (red), and estimates from VOCALS observations (black cross). AM4-MG2 and AM4.0 are sampled over hourly instantaneous three-dimensional autoconversion and accretion rates between [60°S, 60°N] for October and November 2008.

exert larger impacts on liquid clouds. The aerosol indirect effects are thus expected to be stronger, which is confirmed by a more negative RFP (−0.80 W m^{-2} versus −0.62 W m^{-2}) and a more negative shortwave radiative flux perturbation (−0.50 W m^{-2} versus −0.37 W m^{-2}) (See Table 4). Compared to AM4-MG2, AM4-MG2-ExpSed shows weaker precipitation, less removal of cloud water, and stronger aerosol indirect effects on liquid clouds.

In AM4-MG2-IceNucl, the Meyers et al. (1992) ice nucleation scheme that only depends on temperature (Equation 2) is used, rather than the mineral dust and temperature-dependent parameterization following Fan et al. (2019) (Equation 1). The Meyers et al. (1992) scheme generates much more ice crystals (by a factor of 3 or more as shown in Figure 4 in Fan et al. (2019)). More ice crystals result in smaller ice crystal sizes for constant ice water content. Smaller sizes suppress the conversion of ice to snow, because the conversion requires that ice crystal size to reach a threshold (Morrison & Gettelman, 2008). Consequently, more ice remains in the atmosphere. The IWP increases substantially, so does LWCRE (Figures 14b and 14d). Moreover, smaller sizes also lead to the faster WBF process and consume more cloud water, resulting in

Table 5
Comparison of AM4-MG2 and Sensitivity Tests

Name	Sedimentation	Ice nucleation	Horizontal resolution
AM4-MG2	time-implicit	dust and temperature-dependent (Fan et al., 2019)	1º × 1º
AM4-MG2-ExpSed	**explicit (substepping)**	dust and temperature-dependent (Fan et al., 2019)	1º × 1º
AM4-MG2-IceNucl	time-implicit	**temperature-dependent only** (Meyers et al., 1992)	1º × 1º
AM4-MG2-0.5deg	time-implicit	dust and temperature-dependent (Fan et al., 2019)	**0.5° X 0.5°**

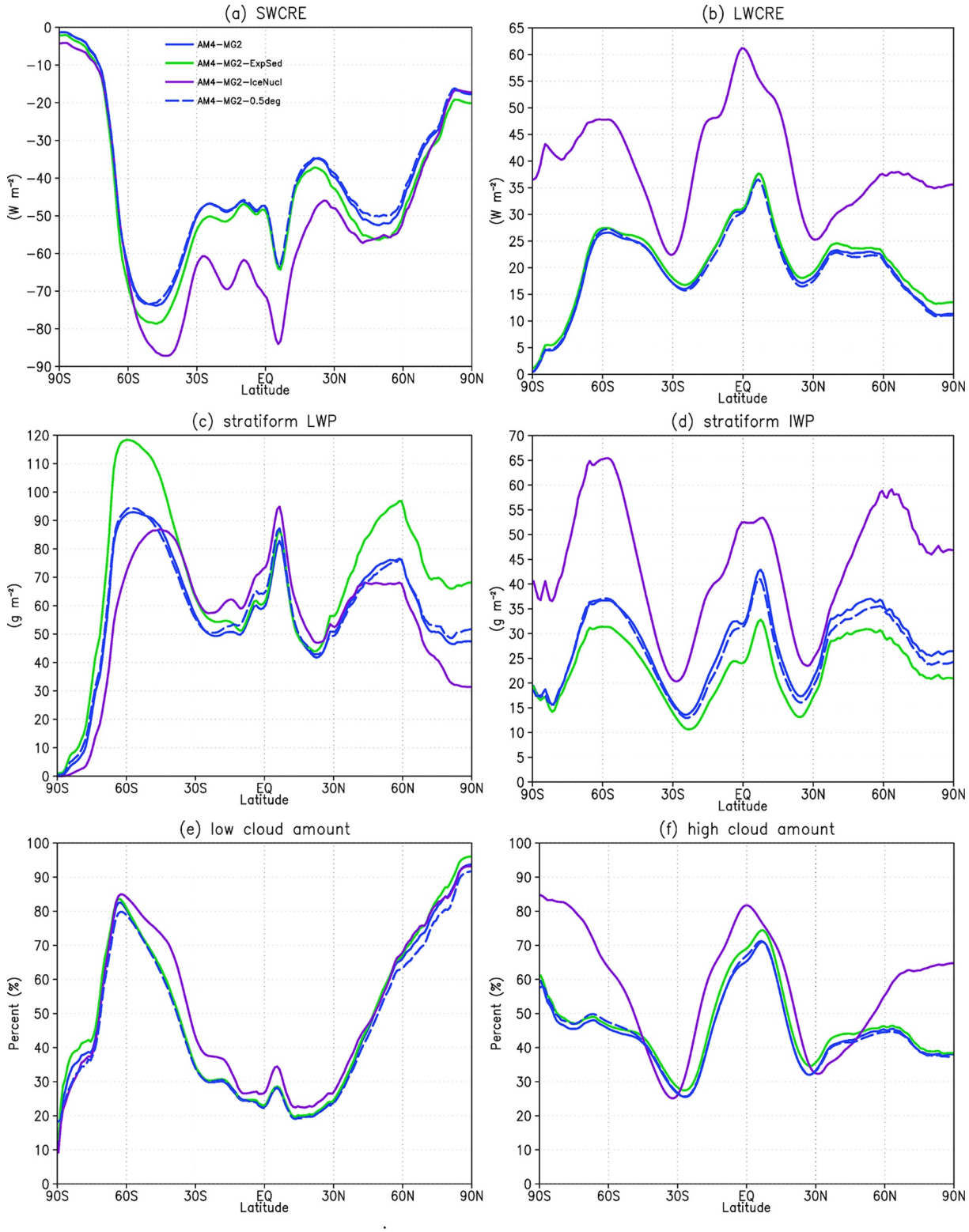

Figure 14. Zonal means of (a) shortwave radiative effect (SWCRE), (b) longwave radiative effect (LWCRE), (c) stratiform liquid water path (LWP), (d) stratiform ice water path (IWP), (e) low cloud amount, and (f) high cloud amount from AM4-MG2, and sensitivity tests with explicit sedimentation scheme (AM4-MG2-ExpSed), with temperature-dependent only ice nucleation scheme (AM4-MG2-IceNucl) (Meyers et al., 1992), with 0.5° × 0.5° degree horizontal resolution (AM4-MG2-0.5deg).

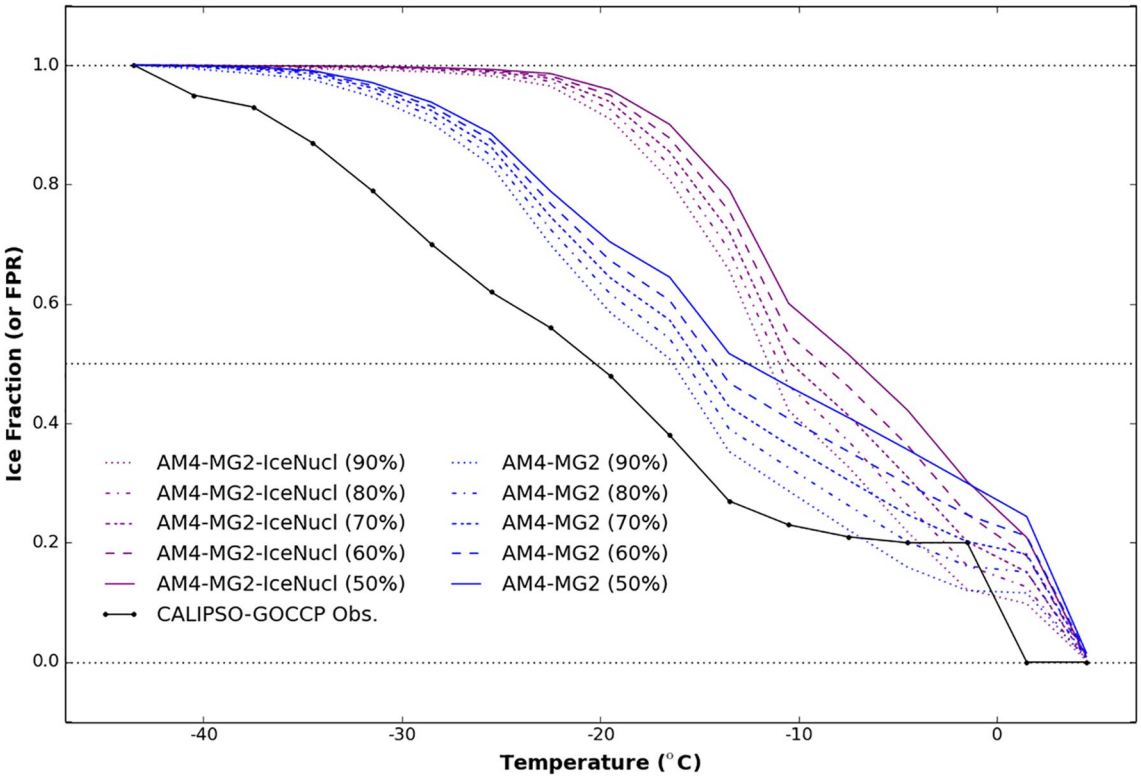

Figure 15. As in Figure 11, but replacing the ice fraction from AM4.0 with that from AM4-MG2-IceNucl. The ice fraction from AM4-MG2-IceNucl is based on daily instantaneous cloud water, ice, and snow fields for 2008.

lower LWP in the mixed-phase regimes of the mid and high latitudes. Less ice sedimentation from above causes less riming of cloud water by ice, and hence higher LWP and low-level cloud amount in the tropics and sub-tropics (Figures 14c and 14e). Considering these changes in the LWP, IWP, and cloud amounts (Figures 14e and 14f), we expect the ice fraction will go up.

Figure 15 shows the ice fractions as a function of temperature from AM4-MG2-IceNucl, AM4-MG2, and the CALIPSO-GOCCP observations (similar to Figure 11). Note that the ice fraction from AM4-MG2-IceNucl is also estimated from daily instantaneous cloud fields for 2008. Compared to the CALIPSO-GOCCP observations, AM4-MG2-IceNucl overestimates the ice fraction. When temperature is colder than −20°C, the ice fraction is almost 1 and much higher than the observations. It then decreases quickly to 0 when temperature is around 0°C. Compared to AM4-MG2, AM4-MG2-IceNucl tends to show higher ice fraction, especially for temperature lower than −10°C. This is consistent with our expectation, and confirms that the ice nucleation parameterizations play an important role in the cloud phase simulations.

In AM4-MG2-0.5deg, we refine the horizontal resolution from 1° (about 100 km) to 0.5° (about 50 km). Unlike AM4-MG2-ExpSed or AM4-MG2-IceNucl, the refined resolution has little impact on the simulated cloud water and ice fields. The LWP declines slightly and the IWP rises a little (Figures 14c and 14d). The weak sensitivity here is in line with Guo et al. (2014). They showed better cloud simulations with higher skill scores in SWCRE and LWCRE when the resolution is increased from 200 to 100 km, but muted changes in cloud fields after the resolution is further increased to 50 km.

6. Summary and Discussion

This paper describes the implementation of the two-moment Morrison-Gettelman bulk cloud microphysics with prognostic precipitation (MG2) and the mineral dust and temperature-dependent ice nucleation scheme in the GFDL AM4.0: AM4-MG2. Various aspects of the global simulation results, including model

mean climate, cloud microphysical and macrophysical properties, have been evaluated against observations and reanalyses.

The model skill scores of AM4-MG2 are comparable to those of AM4.0. More importantly, AM4-MG2 shows improved coastal stratocumulus and seasonal cycles, higher accretion-to-autoconversion ratio, and more realistic ice fraction (or supercooled liquid fraction). These improvements lead to better agreements with satellite and in-situ observations. The better stratocumulus simulations are possibly related to the weaker autoconversion, which is a dominant sink for cloud water especially when the precipitation is diagnostic. The Manton and Cotton (1977) parameterization in AM4.0 is too efficient and removes too much cloud water. As shown in Figure 13b, the AM4.0 autoconversion rate is far above observational estimates, especially for clouds with the LWP lower than 100 g m^{-2}, such as coastal stratocumulus. Meanwhile, AM4-MG2 employs the Seifert and Beheng (2001) autoconversion scheme and prognostic precipitation treatment. They lead to a significant reduction in the autoconversion rate (by a factor of 2 or more), and help sustain the coastal stratocumulus.

Prognostic precipitation decreases the dependence of precipitation on autoconversion and enhances the contribution from accretion, in line with previous studies (Gettelman et al., 2015; Posselt & Lohmann, 2009). Consequently, the rain formation is dominated by accretion, rather than autoconversion. This not only improves the agreement of process rates with in-situ measurements, but also better represents the cloud sensitivity to aerosols, for example, the relationship between the LWP and aerosols (Quaas et al., 2009; Wang et al., 2012). The weaker dependence on autoconversion results in weaker impacts of drop number changes on rain production, and cloud LWP and lifetime. The aerosol radiative flux perturbations are estimated to be −0.62 W m^{-2} in AM4-MG2, about 15% weaker than that in AM4.0.

Prognostic treatment of precipitation does require more computations. The mass mixing ratio and number concentration of rain and snow are subject to large-scale transport and turbulence mixing. Substepping the cloud microphysical processes needs additional costs. These additional costs, however, are partly compensated (about 3%) by replacing the explicit (substepping) sedimentation scheme with the time-implicit one. As a result, the overall computational cost increases by about 10% in AM4-MG2 compared to AM4.0. The increase is affordable given the rapidly growing computational power.

The time-implicit sedimentation scheme is computationally efficient and numerically stable. It speeds up the microphysical module by about 15% in AM4-MG2 at the cost of some additional numerical diffusion. There is a tradeoff between efficiency and accuracy (see Appendix for detailed discussion on the implicit and explicit schemes). At higher resolution with more computational costs, the numerical solutions converge onto exact solutions. At lower spatial and temporal resolution, the implicit scheme does introduce more diffusion in the sedimentation process and is less accurate than the explicit scheme (Figure A1). More diffusion leads to more shift from autoconversion to accretion and thus weaker (or less negative) aerosol RFP than that with the explicit scheme (Table 4). The numerical error of the implicit scheme is a source of uncertainty, although it may not be necessarily more significant than other uncertainties such as hydrometeor fall speed in GCMs which itself has significant spread (Mitchell et al., 2008; Zhao et al., 2013). Furthermore, other desirable characteristics such as exact conservation of the total moist energy make the implicit sedimentation scheme appealing. A variant of the implicit sedimentation scheme, which uses a higher-order Lagrangian remapping method (Lin, 2004) and is thus much more accurate, has been selected for the operational Global Forecast System (GFS) and is used in the GFDL System for High-resolution prediction on Earth-to-Local Domains (SHiELD) (Harris, Zhou, Lin, et al., 2020; Zhou et al., 2019).

The mineral dust and temperature-dependent ice nucleation scheme yields lower ice fractions. The dependency on dust promotes the land-ocean contrast. The ice fraction is higher in the Northern Hemisphere than that in the Southern Hemisphere, which compare favorably with satellite retrievals. The improved partitioning between cloud liquid and ice is encouraging, not only because the cloud phase simulations are challenging due to poorly constrained ice microphysics at the process level (e.g., ice nucleation), but also because the partitioning is closely tied to cloud feedback and climate sensitivity, and in turn influences the current and future climate (Tan et al., 2016; Zelinka et al., 2020).

Assessing the climate sensitivity with AM4-MG2 in the coupled mode will be among key areas of our future work. Future work also involves incorporating the ice nucleation parameterization in the convection,

investigating the longwave radiative flux perturbation caused by anthropogenic aerosols, and further enhancing the subtropical stratocumulus clouds especially along the coasts (e.g., by increasing vertical resolution). AM4-MG2 has been tuned mainly under the "top-down" constraints such as radiative fluxes and precipitation. It has some common biases shared by many GCMs including AM4.0. For example, the LWP is underestimated. The rain formation is too efficient even when cloud drop size is still small. In order to alleviate these biases, "bottom-up" constraints at the process level, such as constraints on the accretion to autoconversion rate, need to be considered for future model development (Held et al., 2019; Jing et al., 2017; Mülmenstädt et al., 2020; Suzuki et al., 2013).

Appendix: Time-Implicit Versus Explicit (Substepping) Sedimentation Schemes

The one-dimensional sedimentation equation can be written as

$$\frac{\partial}{\partial t}q + \frac{\partial}{\partial z}\left(vq\right) = 0 \tag{A1}$$

where q is a hydrometeor species (e.g., rain) and v is its fall velocity (downward positive).

(1) Time-implicit sedimentation scheme

After discretization, the finite difference equation in a time-implicit format is

$$\frac{q_k^{n+1} - q_k^n}{\delta t} = \frac{1}{-\delta z_k}\left(v_k q_k^{n+1} - v_{k-1} q_{k-1}^{n+1}\right) \tag{A2}$$

where δt is time step, and δz_k is the depth of k-th vertical layer. After re-arranging Equation A2, the hydrometeor at the n+1 time step and the k vertical layer (q_k^{n+1}) can be calculated as below

$$q_k^{n+1} = \frac{q_k^n \delta z_k + q_{k-1}^{n+1} v_{k-1} \delta t}{\delta z_k + v_k \delta t} \tag{A3}$$

where $q_1^{n+1} = \frac{q_1^n \delta z_1}{\delta z_1 + v_1 \delta t}$ assuming zero fall velocity at the model top ($k = 1$). It is clear q_k^{n+1} is non-negative. The implicit scheme is conservative and numerically stable regardless of the Courant number.

(2) Explicit (substepping) sedimentation scheme

An explicit upwind discretization can be written as,

$$q_k^{n+1} = \frac{q_k^n \delta z_k - q_k^n v_k \delta t + q_{k-1}^n v_{k-1} \delta t}{\delta z_k} \tag{A4}$$

where $q_1^{n+1} = q_1^n (1 - \frac{v_1 \delta t}{\delta z_1})$ at the model top. There is a chance that q_k^{n+1} becomes negative, which is physically unreasonable, if the Courant number is greater than 1. The explicit scheme is conservative, and numerically stable if the CFL stability criterion is satisfied. This requires substepping (or more computational costs) to keep the Courant number below or equal to 1.

(3) Comparison between the implicit and explicit sedimentation schemes

Both implicit and explicit schemes are first-order accurate. Their truncation errors are $O(\delta t + \delta z)$. In the limit δt and $\delta z \to 0$, the implicit scheme converges to the exact solution. The explicit scheme also converges if the CFL criterion is met.

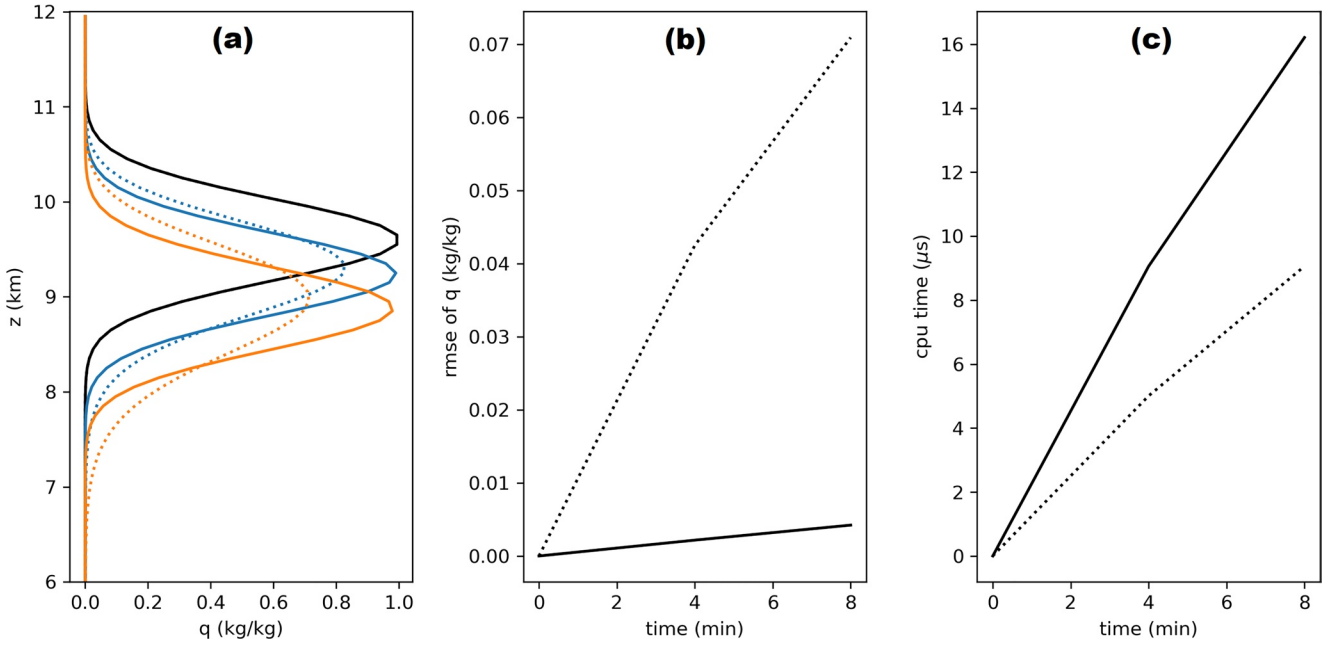

Figure A1. The vertical profiles of rain water content (q) at $t = 0$ min (black), 4 min (blue), and 8 min (orange) with the implicit (dotted) and explicit (solid) schemes in (a), and the time series of root mean square errors (rmse) in (b) and computational cost estimates (i.e., CPU time here) in (c) with the implicit (dotted) and explicit (solid) schemes.

To further compare the performance of both schemes, we conducted an idealized test where rain fell at a constant speed of 1.5 m s^{-1} and the Courant number was 1.8. In this test, the explicit scheme required two substeps but the implicit scheme did not. As shown in Figure A1, both schemes are able to capture the peak and profile. But the implicit scheme smears out the rain water content (Figure A1a). It is more diffusive and shows larger root mean square errors than the explicit scheme (Figure A1b), although it is more computationally efficient (Figure A1c). In other words, higher efficiency in the implicit scheme is achieved at the expense of accuracy.

Data Availability Statement

The AM4.0/LM4.0 source codes are available at http://data1.gfdl.noaa.gov/nomads/forms/am4.0/. The AM4.0 model data have been deposited in the CMIP6 archive with the identifier https://doi.org/10.22033/ESGF/CMIP6.1401. The original MG2 source code was based on the CESM2.1.3 release, which is available at http://www.cesm.ucar.edu/models/cesm2/release_download.html. The AM4-MG2 source codes can be found at https://github.com/NOAA-GFDL/AM4/tree/MG2_xanadu_2020.02.01, or https://doi.org/10.5281/zenodo.4313356. The AM4-MG2 model data can be downloaded at ftp://data1.gfdl.noaa.gov/users/Huan.Guo/microphysics/AM4-MG2/.

The CERES-EBAF and GPCP data can be obtained from https://ceres.larc.nasa.gov/data/and https://psl.noaa.gov/data/gridded/data.gpcp.html, respectively. The TRMM data set can be access from https://disc.gsfc.nasa.gov/datasets/TRMM_3B42_7/summary. (DOI: 10.5067/TRMM/TMPA/3H/7). The GCM Oriented Cloud Calipso Product (CALIPSO-GOCCP) is available at https://climserv.ipsl.polytechnique.fr/cfmip-obs/Calipso_goccp.html

Acknowledgments
The authors thank Dr. Shian-Jiann Lin for designing and sharing the time-implicit sedimentation scheme. The authors also would like to thank two reviewers who helped us to improve the manuscript. Linjiong Zhou is funded under award NA18OAR4320123 from the National Oceanic and Atmospheric Administration, U.S. Department of Commerce. Linjiong Zhou was additionally funded by the Next-Generation Global Prediction System project of the National Weather Service. The National Oceanic and Atmospheric Administration's Hurricane Supplemental Program Office partially funded Linjiong Zhou under award NA19OAR0220147.

References

Adler, R. F., Huffman, G. J., Chang, A., Ferraro, R., Xie, P.-P., Janowiak, J., et al. (2003). The version-2 Global Precipitation Climatology Project (GPCP) monthly precipitation analysis (1979-Present). *Journal of Hydrometeorology*, *4*(6), 1147–1167. https://doi.org/10.1175/1525-7541(2003)004<1147:tvgpcp>2.0.co;2

Adler, R. F., Sapiano, M., Huffman, G., Bolvin, D., Gu, G., Wang, J., et al. (2016). The new version 2.3 of the Global Precipitation Climatology Project (GPCP) monthly analysis product, *Internal Report*, Earth System Science Interdisciplinary Center, Univ. of Maryland, College Park, MD.

Albrecht, B. A. (1989). Aerosols, cloud microphysics, and fractional cloudiness. *Science*, *245*(4923), 1227–1230. https://doi.org/10.1126/science.245.4923.1227

Bower, K. N., & Choularton, T. W. (1992). A parameterization of the effective radius of ice free clouds for use in global climate models. *Atmospheric Research*, *27*(4), 305–339. https://doi.org/10.1016/0169-8095(92)90038-c

Brenguier, J.-L., Pawlowska, H., & Schüller, L. (2003). Cloud microphysical and radiative properties for parameterization and satellite monitoring of the indirect effect of aerosol on climate. *Journal of Geophysical Research*, *108*(D15), 8632. https://doi.org/10.1029/2002JD002682

Brohan, P., Kennedy, J. J., Harris, I., Tett, S. F. B., & Jones, P. D. (2006). Uncertainty estimates in regional and global observed temperature changes: A new data set from 1850. *Journal of Geophysical Research*, *111*(D12). https://doi.org/10.1029/2005JD006548

Cesana, G., Waliser, D. E., Jiang, X., & Li, J. L. F. (2015). Multimodel evaluation of cloud phase transition using satellite and reanalysis data. *Journal of Geophysical Research - D: Atmospheres*, *120*(15), 7871–7892. https://doi.org/10.1002/2014JD022932

Chepfer, H., Bony, S., Winker, D., Cesana, G., Dufresne, J. L., Minnis, P., et al. (2010). The GCM-oriented CALIPSO cloud product (CALIPSO-GOCCP). *Journal of Geophysical Research*, *115*(D4). https://doi.org/10.1029/2009JD012251

Choi, Y.-S., Lindzen, R. S., Ho, C.-H., & Kim, J. (2010). Space observations of cold-cloud phase change. *Proceedings of the National Academy of Sciences*, *107*(25), 11211–11216. https://doi.org/10.1073/pnas.1006241107

Danabasoglu, G., Lamarque, J. F., Bacmeister, J., Bailey, D. A., DuVivier, A. K., Edwards, J., et al. (2020). The community earth system model version 2 (CESM2). *Journal of Advances in Modeling Earth Systems*, *12*(2), e2019MS001916. https://doi.org/10.1029/2019MS001916

Dee, D. P., Uppala, S. M., Simmons, A. J., Berrisford, P., Poli, P., Kobayashi, S., et al. (2011). The ERA-Interim reanalysis: Configuration and performance of the data assimilation system. *Quarterly Journal of the Royal Meteorological Society*, *137*, 553–597. https://doi.org/10.1002/qj.828

Diner, D. J., Beckert, J. C., Reilly, T. H., Bruegge, C. J., Conel, J. E., Kahn, R. A., et al. (1998). Multi-angle Imaging Spectroradiometer (MISR) instrument description and experiment overview. *IEEE Transactions on Geoscience and Remote Sensing*, *36*(4), 1072–1087. https://doi.org/10.1109/36.700992

Donner, L. J., Seman, C. J., Soden, B. J., Hemler, R. S., Warren, J. C., Ström, J., & Liou, K.-N. (1997). Large-scale ice clouds in the gfdl skyhi general circulation model. *Journal of Geophysical Research*, *102*(D18), 21745–21768. https://doi.org/10.1029/97jd01488

Donner, L. J., Wyman, B. L., Hemler, R. S., Horowitz, L. W., Ming, Y., Zhao, M., et al. (2011). The dynamical core, physical parameterizations, and basic simulation characteristics of the atmospheric component AM3 of the GFDL global coupled model CM3. *Journal of Climate*, *24*(13), 3484–3519. https://doi.org/10.1175/2011jcli3955.1

Elsaesser, G. S., O'Dell, C. W., Lebsock, M. D., Bennartz, R., Greenwald, T. J., & Wentz, F. J. (2017). The Multisensor Advanced Climatology of Liquid Water Path (MAC-LWP). *Journal of Climate*, *30*(24), 10193–10210. https://doi.org/10.1175/JCLI-D-16-0902.1

Fan, S., Ginoux, P., Seman, C. J., Silvers, L. G., & Zhao, M. (2019). Toward improved cloud-phase simulation with a mineral dust and temperature-dependent parameterization for ice nucleation in mixed-phase clouds. *Journal of the Atmospheric Sciences*, *76*(11), 3655–3667. https://doi.org/10.1175/JAS-D-18-0287.1

Fan, S., Knopf, D. A., Heymsfield, A. J., & Donner, L. J. (2017). Modeling of aircraft measurements of ice crystal concentration in the Arctic and a parameterization for mixed-phase cloud. *Journal of the Atmospheric Sciences*, *74*, 3799–3814. https://doi.org/10.1175/JAS-D-17-0037.1

Fu, Q., Krueger, S. K., & Liou, K. N. (1995). Interactions of radiation and convection in simulated tropical cloud clusters. *Journal of the Atmospheric Sciences*, *52*(9), 1310–1328. https://doi.org/10.1175/1520-0469(1995)052<1310:ioraci>2.0.co;2

Garner, S. T. (2005). A topographic drag closure built on an analytical base flux. *Journal of the Atmospheric Sciences*, *62*(7), 2302–2315. https://doi.org/10.1175/jas3496.1

Garner, S. T. (2018). Ground-truth model evaluation of subgrid orographic base-flux parameterization. *Journal of the Atmospheric Sciences*, *75*(10), 3653–3670. https://doi.org/10.1175/jas-d-17-0368.1

Gates, W. L. (1992). AMIP: The Atmospheric Model Intercomparison Project. *Bulletin of the American Meteorological Society*, *73*(12), 1962–1970. https://doi.org/10.1175/1520-0477(1992)073<1962:atamip>2.0.co;2

Gates, W. L., Boyle, J. S., Covey, C., Dease, C. G., Doutriaux, C. M., Drach, R. S., et al. (1999). An overview of the results of the Atmospheric Model Intercomparison Project (AMIP I). *Bulletin of the American Meteorological Society*, *80*, 29–55. https://doi.org/10.1175/1520-0477(1999)080<0029:aootro>2.0.co;2

Gehne, M., Hamill, T. M., Kiladis, G. N., & Trenberth, K. E. (2016). Comparison of global precipitation estimates across a range of temporal and spatial scales. *Journal of Climate*, *29*(21), 7773–7795. https://doi.org/10.1175/JCLI-D-15-0618.1

Gettelman, A., & Morrison, H. (2015). Advanced two-moment bulk microphysics for global models. Part I: Off-line tests and comparison with other schemes. *Journal of Climate*, *28*(3), 1268–1287. https://doi.org/10.1175/JCLI-D-14-00103.110.1175/jcli-d-14-00102.1

Gettelman, A., Morrison, H., & Ghan, S. J. (2008). A new two-moment bulk stratiform cloud microphysics scheme in the Community Atmosphere Model, version 3 (CAM3). Part II: Single-column and global results. *Journal of Climate*, *21*, 3660–3679. https://doi.org/10.1175/2008JCLI2116.1

Gettelman, A., Morrison, H., Santos, S., Bogenschutz, P., & Caldwell, P. M. (2015). Advanced Two-Moment Bulk Microphysics for Global Models. Part II: Global Model Solutions and Aerosol-Cloud Interactions. *Journal of Climate*, *28*(3), 1288–1307. https://doi.org/10.1175/JCLI-D-14-00102.110.1175/jcli-d-14-00103.1

Gettelman, A., Morrison, H., Terai, C. R., & Wood, R. (2013). Microphysical process rates and global aerosol-cloud interactions. *Atmospheric Chemistry and Physics*, *13*(11), 11789–11825. https://doi.org/10.5194/acpd-13-11789-2013

GFDL Global Atmosphere Model Development Team. (2004). The new GFDL global atmosphere and land model AM2-LM2: Evaluation with prescribed SST simulations. *Journal of Climate*, *17*, 4641–4673. https://doi.org/10.1175/JCLI-3223.1

Ghan, S. J., Abdul-Razzak, H., Nenes, A., Ming, Y., Liu, X., Ovchinnikov, M., et al. (2011). Droplet nucleation: Physically-based parameterizations and comparative evaluation. *Journal of Advances in Modeling Earth Systems*, *3*(4). https://doi.org/10.1029/2011MS000074

Ghan, S. J., Leung, L. R., Easter, R. C., & Abdul-Razzak, H. (1997). Prediction of cloud droplet number in a general circulation model. *Journal of Geophysical Research*, *102*(D18), 21777–21794. https://doi.org/10.1029/97JD01810

Golaz, J.-C., Caldwell, P. M., Van Roekel, L. P., Petersen, M. R., Tang, Q., Wolfe, J. D., et al. (2019). The DOE E3SM coupled model version 1: Overview and evaluation at standard resolution. *Journal of Advances in Modeling Earth Systems*, *11*, 2089–2129. https://doi.org/10.1029/2018MS001603

Golaz, J.-C., Salzmann, M., Donner, L. J., Horowitz, L. W., Ming, Y., & Zhao, M. (2011). Sensitivity of the aerosol indirect effect to subgrid variability in the cloud parameterization of the gfdl atmosphere general circulation model AM3. *Journal of Climate*, *24*, 3145–3160. https://doi.org/10.1175/2010JCLI3945.1

Gordon, C. T., Rosati, A., & Gudgel, R. (2000). Tropical sensitivity of a coupled model to specified ISCCP low clouds. *Journal of Climate*, *13*(13), 2239–2260. https://doi.org/10.1175/1520-0442(2000)013<2239:tsoacm>2.0.co;2

Gultepe, I., & Isaac, G. A. (2004). Aircraft observations of cloud droplet number concentration: Implications for climate studies. *Quarterly Journal of the Royal Meteorological Society*, *130*, 2377–2390. https://doi.org/10.1256/qj.03.120

Guo, H., Golaz, J.-C., Donner, L. J., Ginoux, P., & Hemler, R. S. (2014). Multivariate probability density functions with dynamics in the GFDL atmospheric general circulation model: Global tests. *Journal of Climate*, *27*(5), 2087–2108. https://doi.org/10.1175/JCLI-D-13-00347.1

Harris, L., Zhou, L., Chen, X., & Chen, J.-H. (2020a). The GFDL finite-volume cubed-sphere dynamical core. *NOAA Technical Memorandum*. https://doi.org/10.25923/7h88-c534

Harris, L., Zhou, L., Lin, S. J., Chen, J. H., Chen, X., Gao, K., et al. (2020b). GFDL SHiELD: A unified system for weather-to-seasonal prediction. *Journal of Advances in Modeling Earth Systems*, *12*, e2020MS002223. https://doi.org/10.1029/2020MS002223

Haywood, J., Donner, L., Jones, A., & Golaz, J.-C. (2009). Global indirect radiative forcing caused by aerosols. In J. Heintzenberg, & R. J. Charlson (Eds.), *Clouds in the perturbed climate system: Their relationship to energy balance, atmospheric dynamics, and precipitation* (pp. 451–468). MIT Press. https://doi.org/10.7551/mitpress/9780262012874.003.0019

Held, I. M., Guo, H., Adcroft, A., Dunne, J. P., Horowitz, L. W., Krasting, J., et al. (2019). Structure and Performance of GFDL's CM4.0 Climate Model. *Journal of Advances in Modeling Earth Systems*, *11*(11), 3691–3727. https://doi.org/10.1029/2019MS001829

Heymsfield, A. J., & Platt, C. M. R. (1984). A parameterization of the particle size spectrum of ice clouds in terms of the ambient temperature and the ice water content. *Journal of the Atmospheric Sciences*, *41*(5), 846–855. https://doi.org/10.1175/1520-0469(1984)041<0846:apotps>2.0.co;2

Hoose, C., Lohmann, U., Edin, R., & Tegen, I. (2008). Global influence of dust mineralogical composition on heterogeneous ice nucleation in mixed-phase clouds. *Environmental Research Letters*, *3*(2), 025003. https://doi.org/10.1088/1748-9326/3/2/025003

Hoose, C., & Möhler, O. (2012). Heterogeneous ice nucleation on atmospheric aerosols: A review of results from laboratory experiments. *Atmospheric Chemistry and Physics*, *12*, 9817–9854. https://doi.org/10.5194/acp-12-9817-2012

Horowitz, L. W., Naik, V., Paulot, F., Ginoux, P. A., Dunne, J. P., Mao, J., et al. (2020). The GFDL global atmospheric chemistry-climate model AM4.1: Model description and simulation characteristics. *Journal of Advances in Modeling Earth Systems*, *12*, e2019MS002032. https://doi.org/10.1029/2019MS002032

Hu, Y., Rodier, S., Xu, K.-m., Sun, W., Huang, J., Lin, B., et al. (2010). Occurrence, liquid water content, and fraction of supercooled water clouds from combined caliop/iir/modis measurements. *Journal of Geophysical Research*, *115*(D4). https://doi.org/10.1029/2009JD012384

Huffman, G. J., Bolvin, D. T., Nelkin, E. J., Wolff, D. B., Adler, R. F., Gu, G., et al. (2007). The TRMM multisatellite precipitation analysis (TMPA): Quasi-global, multiyear, combined-sensor precipitation estimates at fine scales. *Journal of Hydrometeorology*, *8*, 38–55. https://doi.org/10.1175/JHM560.1

IPCC. (2013). Climate Change 2013: The Physical Science Basis. In T. F. Stocker (Ed.), *Contribution of working Group I to the fifth assessment report of the intergovernmental panel on climate change*. Cambridge University Press.

Jakob, C., & Klein, S. A. (2000). A parametrization of the effects of cloud and precipitation overlap for use in general-circulation models. *Quarterly Journal of the Royal Meteorological Society*, *126*, 2525–2544. https://doi.org/10.1002/qj.49712656809

Jiang, J. H., Su, H., Zhai, C., Perun, V. S., Del Genio, A., Nazarenko, L. S., et al. (2012). Evaluation of cloud and water vapor simulations in CMIP5 climate models using NASA "A-Train" satellite observations. *Journal of Geophysical Research*, *117*. https://doi.org/10.1029/2011JD017237

Jing, X., Suzuki, K., Guo, H., Goto, D., Ogura, T., Koshiro, T., & Mülmenstädt, J. (2017). A multimodel study on warm precipitation biases in global models compared to satellite observations. *Journal of Geophysical Research - D: Atmospheres*, *122*, 11806–11824. https://doi.org/10.1002/2017JD027310

Jolliff, J. K., Kindle, J. C., Shulman, I., Penta, B., Friedrichs, M. A. M., Helber, R., & Arnone, R. A. (2009). Summary diagrams for coupled hydrodynamic-ecosystem model skill assessment. *Journal of Marine Systems*, *76*, 64–82. https://doi.org/10.1016/j.jmarsys.2008.05.014

Kahn, R. A., Gaitley, B. J., Martonchik, J. V., Diner, D. J., Crean, K. A., & Holben, B. (2005). Multiangle Imaging Spectroradiometer (MISR) global aerosol optical depth validation based on 2 years of coincident Aerosol Robotic Network (AERONET) observations. *Journal of Geophysical Research*, *110*. D10S04. https://doi.org/10.1029/2004JD004706

Kahn, R. A., Nelson, D. L., Garay, M. J., Levy, R. C., Bull, M. A., Diner, D. J., et al. (2009). MISR aerosol product attributes and statistical comparisons with MODIS. *IEEE Transactions on Geoscience and Remote Sensing*, *47*, 4095–4114. https://doi.org/10.1109/TGRS.2009.2023115

Kato, S., Sun-Mack, S., Miller, W. F., Rose, F. G., Chen, Y., Minnis, P., & Wielicki, B. A. (2010). Relationships among cloud occurrence frequency, overlap, and effective thickness derived from CALIPSO and CloudSat merged cloud vertical profiles. *Journal of Geophysical Research*, *115*(D00H28), 6521–6533. https://doi.org/10.1029/2009JD012277

Kelley, M., Schmidt, G. A., Nazarenko, L. S., Bauer, S. E., Ruedy, R., Russell, G. L., et al. (2020). GISS-E2.1: Configurations and climatology. *Journal of Advances in Modeling Earth Systems*, *12*(8). https://doi.org/10.1029/2019MS002025

Klein, S. A., & Hartmann, D. L. (1993). The seasonal cycle of low stratiform clouds. *Journal of Climate*, *6*, 1587–1606. https://doi.org/10.1175/1520-0442(1993)006<1587:tscols>2.0.co;2

Komurcu, M., Storelvmo, T., Tan, I., Lohmann, U., Yun, Y., Penner, J. E., et al. (2014). Intercomparison of the cloud water phase among global climate models. *Journal of Geophysical Research - D: Atmospheres*, *119*, 3372–3400. https://doi.org/10.1002/2013JD021119

Koop, T., Luo, B., Tsias, A., & Peter, T. (2000). Water activity as the determinant for homogeneous ice nucleation in aqueous solutions. *Nature*, *406*(6796), 611–614. https://doi.org/10.1038/35020537

Kristjansson, J. E., Edwards, J. M., & Mitchell, D. L. (2000). Impact of a new scheme for optical properties of ice crystals on climates of two gcms. *Journal of Geophysical Research*, *105*(D8), 10063–10079. https://doi.org/10.1029/2000jd900015

Large, W. G., & Danabasoglu, G. (2006). Attribution and impacts of upper-ocean biases in CCSM3. *Journal of Climate*, *19*(11), 2325–2346. https://doi.org/10.1175/JCLI3740.1

Lin, S.-J. (2004). A "Vertically Lagrangian" finite-volume dynamical core for global models. *Monthly Weather Review*, *132*(10), 2293–2307. https://doi.org/10.1175/1520-0493(2004)132<2293:avlfdc>2.0.co;2

Lock, A. P., Brown, A. R., Bush, M. R., Martin, G. M., & Smith, R. N. B. (2000). A new boundary layer mixing scheme. Part I: Scheme description and single-column model tests. *Monthly Weather Review*, *128*, 3187–3199. https://doi.org/10.1175/1520-0493(2000)128<3187:anblms>2.0.co;2

Loeb, N. G., Doelling, D. R., Wang, H., Su, W., Nguyen, C., Corbett, J. G., et al. (2018). Clouds and the Earth's Radiant Energy System (CERES) Energy Balanced and Filled (EBAF) Top-of-Atmosphere (TOA) Edition-4.0 data product. *Journal of Climate*, *31*(2), 895–918. https://doi.org/10.1175/jcli-d-17-0208.1

Loeb, N. G., Wielicki, B. A., Doelling, D. R., Smith, G. L., Keyes, D. F., Kato, S., et al. (2009). Toward optimal closure of the earth's top-of-atmosphere radiation budget. *Journal of Climate*, *22*(3), 748–766. https://doi.org/10.1175/2008jcli2637.1

Lohmann, U., Feichter, J., Chuang, C. C., & Penner, J. E. (1999). Prediction of the number of cloud droplets in the ECHAM GCM. *Journal of Geophysical Research*, *104*(D8), 9169–9198. https://doi.org/10.1029/1999JD900046

Lohmann, U., Rotstayn, L., Storelvmo, T., Jones, A., Menon, S., Quaas, J., et al. (2010). Total aerosol effect: Radiative forcing or radiative flux perturbation? *Atmospheric Chemistry and Physics*, *10*, 3235–3246. https://doi.org/10.5194/acp-10-3235-2010

Ma, P.-L., Rasch, P. J., Wang, M., Wang, H., Ghan, S. J., Easter, R. C., et al. (2015). How does increasing horizontal resolution in a global climate model improve the simulation of aerosol-cloud interactions? *Geophysical Research Letters*, *42*(12), 5058–5065. https://doi.org/10.1002/2015GL064183

Manton, M. J., & Cotton, W. R. (1977), Formulation of approximate equations for modeling moist deep convection on the mesoscale, *Atmospheric Science Paper No. 266*, Colorado State University, Fort Collins, CO.

Martin, G. M., Johnson, D. W., & Spice, A. (1994). The measurement and parameterization of effective radius of droplets in warm stratocumulus clouds. *Journal of the Atmospheric Sciences*, *51*, 1823–1842. https://doi.org/10.1175/1520-0469(1994)051<1823:tmapoe>2.0.co;2

McCoy, D. T., Tan, I., Hartmann, D. L., Zelinka, M. D., & Storelvmo, T. (2016). On the relationships among cloud cover, mixed-phase partitioning, and planetary albedo in gcms. *Journal of Advances in Modeling Earth Systems*, *8*, 650–668. https://doi.org/10.1002/2015MS000589

Meyers, M. P., DeMott, P. J., & Cotton, W. R. (1992). New primary ice-nucleation parameterizations in an explicit cloud model. *Journal of Applied Meteorology*, *31*, 708–721. https://doi.org/10.1175/1520-0450(1992)031<0708:npinpi>2.0.co;2

Ming, Y., Ramaswamy, V., Donner, L. J., & Phillips, V. T. J. (2006). A new parameterization of cloud droplet activation applicable to General Circulation Models. *Journal of the Atmospheric Sciences*, *63*, 1348–1356. https://doi.org/10.1175/jas3686.1

Ming, Y., Ramaswamy, V., Donner, L. J., Phillips, V. T. J., Klein, S. A., Ginoux, P. A., & Horowitz, L. W. (2007). Modeling the interactions between aerosols and liquid water clouds with a self-consistent cloud scheme in a General Circulation Model. *Journal of the Atmospheric Sciences*, *64*(4), 1189–1209. https://doi.org/10.1175/JAS3874.1

Mitchell, D. L., Rasch, P., Ivanova, D., McFarquhar, G., & Nousiainen, T. (2008). Impact of small ice crystal assumptions on ice sedimentation rates in cirrus clouds and GCM simulations. *Geophysical Research Letters*, *35*, L09806. https://doi.org/10.1029/2008GL033552

Morrison, H., & Gettelman, A. (2008). A new two-moment bulk stratiform cloud microphysics scheme in the Community Atmosphere Model, version 3 (CAM3). Part I: Description and numerical tests. *Journal of Climate*, *21*, 3642–3659. https://doi.org/10.1175/2008JCLI2105.1

Mülmenstädt, J., Nam, C., Salzmann, M., Kretzschmar, J., L'Ecuyer, T. S., Lohmann, U., et al. (2020). Reducing the aerosol forcing uncertainty using observational constraints on warm rain processes. *Science Advances*, *6*(22), eaaz6433. https://doi.org/10.1126/sciadv.aaz6433

Niemand, M., Möhler, O., Vogel, B., Vogel, H., Hoose, C., Connolly, P., et al. (2012). A particle-surface-area-based parameterization of immersion freezing on desert dust particles. *Journal of the Atmospheric Sciences*, *69*, 3077–3092. https://doi.org/10.1175/JAS-D-11-0249.1

Niu, S., Jia, X., Sang, J., Liu, X., Lu, C., & Liu, Y. (2010). Distributions of raindrop sizes and fall velocities in a semiarid plateau climate: Convective versus stratiform rains, *Journal of Applied Meteorology and Climatology*, *49*(4), 632–645. https://doi.org/10.1175/2009JAMC2208.1

Pawlowska, H., Grabowski, W. W., & Brenguier, J. L. (2006). Observations of the width of cloud droplet spectra in stratocumulus. *Geophysical Research Letters*, *33*. L19810. https://doi.org/10.1029/2006GL026841

Pincus, R., Buehler, S. A., Brath, M., Crevoisier, C., Jamil, O., Franklin Evans, K., et al. (2020). Benchmark calculations of radiative forcing by greenhouse gases. *Journal of Geophysical Research - D: Atmospheres*, *125*, e2020JD033. https://doi.org/10.1029/2020JD033483

Posselt, R., & Lohmann, U. (2008). Introduction of prognostic rain in ECHAM5: Design and single column model simulations. *Atmospheric Chemistry and Physics*, *8*, 2949–2963. https://doi.org/10.5194/acp82949200810.5194/acp-8-2949-2008

Posselt, R., & Lohmann, U. (2009). Sensitivity of the total anthropogenic aerosol effect to the treatment of rain in a global climate model. *Geophysical Research Letters*, *36*, L02805. https://doi.org/10.1029/2008GL035796

Putman, W. M., & Lin, S.-J. (2007). Finite-volume transport on various cubed-sphere grids. *Journal of Computational Physics*, *227*(1), 55–78. https://doi.org/10.1016/j.jcp.2007.07.022

Quaas, J., Ming, Y., Menon, S., Takemura, T., Wang, M., Penner, J. E., et al. (2009). Aerosol indirect effects - general circulation model intercomparison and evaluation with satellite data. *Atmospheric Chemistry and Physics*, *9*, 8697–8717. https://doi.org/10.5194/acp-9-8697-2009

Rotstayn, L. D. (1997). A physically based scheme for the treatment of stratiform clouds and precipitation in large-scale models. I: Description and evaluation of the microphysical processes. *Quarterly Journal of the Royal Meteorological Society*, *123*, 1227–1282. https://doi.org/10.1002/qj.49712354106

Rotstayn, L. D., Ryan, B. F., & Katzfey, J. J. (2000). A scheme for calculation of the liquid fraction in mixed-phase stratiform clouds in large-scale models. *Monthly Weather Review*, *128*, 1070–1088. https://doi.org/10.1175/1520-0493(2000)128<1070:asfcot>2.0.co;2

Salzmann, M., Ming, Y., Golaz, J.-C., Ginoux, P. A., Morrison, H., Gettelman, A., et al. (2010). Two-moment bulk stratiform cloud microphysics in the gfdl am3 gcm: Description, evaluation, and sensitivity tests. *Atmospheric Chemistry and Physics*, *10*(16), 8037–8064. https://doi.org/10.5194/acp108037201010.5194/acp-10-8037-2010

Savijärvi, H. (1997). Short-wave optical properties of rain. *Tellus A*, *49*(2), 177–181. https://doi.org/10.3402/tellusa.v49i2.14463

Seifert, A., & Beheng, K. D. (2001). A double-moment parameterization for simulating autoconversion, accretion and selfcollection. *Atmospheric Research*, *59–60*, 265–281. https://doi.org/10.1016/s0169-8095(01)00126-0

Stephens, G., Li, J., Wild, M., Clayson, C. A., Loeb, N., Kato, S., et al. (2012). An update on Earth's energy balance in light of the latest global observations. *Nature Geoscience*, *5*, 691–696. https://doi.org/10.1038/NGEO1580

Sui, C.-H., Li, X., & Yang, M.-J. (2007). On the definition of precipitation efficiency. *Journal of the Atmospheric Sciences*, *64*, 4506–4513. https://doi.org/10.1175/2007JAS2332.1

Sui, C.-H., X. Li, M.-J. Yang, and H.-L. Huang, (2005). Estimation of oceanic precipitation efficiency in cloud models, *Journal of the Atmospheric Sciences*, *62*(12), 4358–4370, https://doi.org/10.1175/JAS3587.1

Sun, Q., Miao, C., Duan, Q., Ashouri, H., Sorooshian, S., & Hsu, K. L. (2018). A review of global precipitation data sets: Data sources, estimation, and intercomparisons. *Reviews of Geophysics*, *56*, 79–107. https://doi.org/10.1002/2017RG000574

Suzuki, K., Golaz, J. C., & Stephens, G. L. (2013). Evaluating cloud tuning in a climate model with satellite observations. *Geophysical Research Letters*, *40*(16), 4464–4468. https://doi.org/10.1002/grl.50874

Tan, I., Storelvmo, T., & Choi, Y.-S. (2014). Spaceborne lidar observations of the ice-nucleating potential of dust, polluted dust, and smoke aerosols in mixed-phase clouds. *Journal of Geophysical Research - D: Atmospheres*, *119*(11), 6653–6665. https://doi.org/10.1002/2013JD021333

Tan, I., Storelvmo, T., & Zelinka, M. D. (2016). Observational constraints on mixed-phase clouds imply higher climate sensitivity. *Science*, *352*, 224–227. https://doi.org/10.1126/science.aad5300

Tiedtke, M. (1993). Representation of clouds in large-scale models. *Monthly Weather Review*, *121*(121), 3040–3061. https://doi.org/10.1175/1520-0493(1993)121<3040:rocils>2.0.co;2

Twomey, S. (1974). Pollution and the planetary albedo. *Atmospheric Environment*, *8*, 1251–1256. https://doi.org/10.1016/0004-6981(74)90004-3

Ullrich, R., Hoose, C., Cziczo, D. J., Froyd, K. D., Schwarz, J. P., Perring, A. E., et al. (2019). Comparison of modeled and measured ice nucleating particle composition in a cirrus cloud. *Journal of the Atmospheric Sciences*, *76*(4), 1015–1029. https://doi.org/10.1175/JAS-D-18-0034.1

Ullrich, R., Hoose, C., Möhler, O., Niemand, M., Wagner, R., Höhler, K., et al. (2017). A new ice nucleation active site parameterization for desert dust and soot. *Journal of the Atmospheric Sciences*, *74*(3), 699–717. https://doi.org/10.1175/JAS-D-16-0074.1

Uppala, S. M., KÅllberg, P. W., Simmons, A. J., Andrae, U., Bechtold, V. D. C., Fiorino, M., et al. (2005). The ERA40 re-analysis, *Quarterly Journal of the Royal Meteorological Society*, *131*, 2961–3012. https://doi.org/10.1256/qj.04.176

Voldoire, A., Saint-Martin, D., Sénési, S., Decharme, B., Alias, A., Chevallier, M., et al. (2019). Evaluation of CMIP6 DECK experiments with CNRM-CM6-1. *Journal of Advances in Modeling Earth Systems*, *11*, 2177–2213. https://doi.org/10.1029/2019MS001683

Walters, D. N., Williams, K. D., Boutle, I. A., Bushell, A. C., Edwards, J. M., Field, L. A. P., et al. (2014). The met office unified model global atmosphere 4.0 and jules global land 4.0 configurations, *Geosci. Model Developments*, *7*, 361–386. https://doi.org/10.5194/gmd7361201410.5194/gmd-7-361-2014

Wang, M., Ghan, S., Liu, X., L'Ecuyer, T. S., Zhang, K., Morrison, H., et al. (2012). Constraining cloud lifetime effects of aerosols using A-Train satellite observations. *Geophysical Research Letters*, *39*. L15709. https://doi.org/10.1029/2012GL052204

Wood, R., Mechoso, C. R., Bretherton, C. S., Weller, R. A., Huebert, B., Straneo, F., et al. (2011). The vamos ocean–cloud– atmosphere–land study regional experiment (vocalsrex): Goals, platforms, and field operations. *Atmospheric Chemistry and Physics*, *11*, 627–654. https://doi.org/10.5194/acp-11-627-2011

Zelinka, M. D., Myers, T. A., McCoy, D. T., Po-Chedley, S., Caldwell, P. M., Ceppi, P., et al. (2020). Causes of higher climate sensitivity in cmip6 models. *Geophysical Research Letters*, *47*, e2019GL085782. https://doi.org/10.1029/2019GL085782

Zhao, C., Liu, X., Qian, Y., Yoon, J., Hou, Z., Lin, G., et al. (2013). A sensitivity study of radiative fluxes at the top of atmosphere to cloud-microphysics and aerosol parameters in the community atmosphere model CAM5. *Atmospheric Chemistry and Physics*, *13*(21), 10969–10987. https://doi.org/10.5194/acp-1310969201310.5194/acp-13-10969-2013

Zhao, M. (2014). An investigation of the connections among convection, clouds, and climate sensitivity in a global climate model. *Journal of Climate*, *27*(5), 1845–1862. https://doi.org/10.1175/JCLID1300145.110.1175/jcli-d-13-00145.1

Zhao, M., Golaz, J.-C., Held, I., Guo, H., Balaji, V., Benson, R., et al. (2018a). The GFDL global atmosphere and land model AM4. 0/LM4.0-Part I: Simulation characteristics with prescribed SSTs. *Journal of Advances in Modeling Earth Systems*, *10*(3), 691–734. https://doi.org/10.1002/2017ms001208

Zhao, M., Golaz, J.-C., Held, I., Guo, H., Balaji, V., Benson, R., et al. (2018b). The GFDL global atmosphere and land model AM4. 0/LM4.0-Part II: Model description, sensitivity studies, and tuning strategies. *Journal of Advances in Modeling Earth Systems*, *10*(3), 735–769. https://doi.org/10.1002/2017ms001209

Zhao, M., Golaz, J.-C., Held, I. M., Ramaswamy, V., Lin, S.-J., Ming, Y., et al. (2016). Uncertainty in model climate sensitivity traced to representations of cumulus precipitation microphysics. *Journal of Climate*, *29*(2), 543–560. https://doi.org/10.1175/JCLI-D-15-0191.1

Zhao, M., Held, I. M., Lin, S.-J., & Vecchi, G. A. (2009). Simulations of global hurricane climatology, interannual variability, and response to global warming using a 50-km resolution GCM. *Journal of Climate*, *22*(24), 6653–6678. https://doi.org/10.1175/2009jcli3049.1

Zhou, L., Lin, S.-J., Chen, J.-H., Harris, L., Chen, X., & Rees, S. L. (2019). Toward convective-scale prediction within the next generation global prediction system. *Bulletin of the American Meteorological Society*, *100*(7), 1225–1243. https://doi.org/10.1175/BAMS-D-17-0246.1